International Reviews in Physical Chemistry
Vol. 27, No. 1, January–March 2008, 53–85

Taylor & Francis
Taylor & Francis Group

Photoelectron imaging of negative ions

Andrei Sanov[a]* and Richard Mabbs[b]

[a]*Department of Chemistry, University of Arizona, Tucson, AZ 85721-0041, USA;* [b]*Department of Chemistry, Washington University, St. Louis, MO 63130-4899, USA*

(*Received 5 September 2007; final version received 5 November 2007*)

This article provides an overview of some of the recent advances in the rapidly growing field of negative-ion photoelectron imaging spectroscopy. Setting the work that spans several projects in the authors' laboratory in broader context, three types of measurements are described. First are the 'static' (one-photon) photoelectron imaging experiments that aim to characterize the electronic structure and photodetachment dynamics of negative ions, providing 'signatures' of the bound electron orbitals. The experimental results are presented alongside a conceptual symmetry-based description of the photodetachment processes, enabling a qualitative interpretation of the photoelectron images. Second, the effects of solvation on the electronic structure and photodetachment dynamics are examined using photoelectron imaging of cluster anions. Third, the time-resolved experiments that target imaging of bond dissociation, as viewed from the electronic perspective along the time-resolved reaction coordinate, are described in the context of dual centre interference in molecular-anion photodetachment.

Keywords: femtosecond time-resolved spectroscopy; negative ions; photoelectron imaging; photoelectron spectroscopy

Contents

*Corresponding author. Email: sanov@u.arizona.edu

ISSN 0144–235X print/ISSN 1366–591X online

DOI: 10.1080/01442350701786512
http://www.informaworld.com

1. Introduction

In recent years, photoelectron imaging[1–3] has grown into a widely used technique of photoelectron spectroscopy, particularly for negative ions.[4] This has been a truly remarkable development, considering that at the turn of this century very few examples of anion photoelectron imaging experiments had been reported.[5,6] The widespread application of photoelectron imaging[5,7–15] was propelled by the development of velocity-mapping.[16,17] This surprisingly simple instrumental approach, which nonetheless revolutionized the imaging technique,[18] offers exceptional energy resolution, alongside the simultaneous measurement of the angular distributions.

Shortly after the advent of velocity-mapping, several groups realized its potential in the challenging field of negative ions.[8,10,11,19–25] The initial successes prompted broader applications and (in our admittedly subjective view) photoelectron imaging has overtaken many other approaches to anion photoelectron spectroscopy in its widespread use and impact. This paper offers two investigators' personal perspective of some of the recent accomplishments in this rapidly growing field. The review is by no means comprehensive, as it is based mainly on the authors' own results, pulling together work that has spanned several years of experimentation and many regular journal articles. The principal goal of the present article is to provide an overview of this work and set it in broader context.

The high impact of photoelectron imaging is due to its effectiveness in advancing the principal goal of photoelectron spectroscopy: the attainment of an electron-centred view of chemical bonding and reactivity. The bonding is controlled by electrons, and it is their dynamics that determine the potential energy landscapes and ultimately control the molecular structures and reaction outcomes. The experiments described here fall loosely into the following categories:

(1) characterization of the electronic structure and photodetachment dynamics of negative ions, using photoelectron images as 'signatures' of the bound electron orbitals;
(2) studies of intermolecular interactions and their effects on the photodetachment of cluster anions;
(3) time-resolved studies of anionic reactivity, focusing on the electronic-structural aspects of bond breaking and the photodetachment dynamics of excited molecular systems in the process of chemical change.

The practical importance and rich fundamental properties of negative ions make them appealing targets for studies of chemical reactivity at the molecular-orbital level. Anions are implicated in many natural and technological chemical processes. As many common and important chemical processes involve ionic reactions, the reactivity of anions and their isolated properties are vital to understanding chemistry of solutions, as well as bio- and environmental chemistry.[26,27] The reactivity of anions is affected by strong interactions with the environment. Not only are these interactions stronger than the van der Waals forces between neutrals, but they are particularly relevant in chemistry, as the diffuse nature of anionic orbitals renders the excess electron both an active player in chemical dynamics and a sensitive probe thereof.

The *intra*molecular behaviour of electrons in negative ions and the photodetachment dynamics also differ significantly from the corresponding phenomena in neutral species.[4] For example, whereas the dynamics of a highly excited electron in a neutral atom or molecule are shaped by the strong interactions with the positively charged core, an excited electron in a negative ion interacts rather weakly with the neutral skeleton, which drastically limits the number of bound anionic states. This also makes the photodetachment process, as well as the excited-state dynamics below the detachment threshold, more sensitive to external perturbations, and thus one finds the photodetachment of negative ions to be a sensitive probe of chemistry.

From the *experimental* perspective, anions allow the preparation and mass-selection of solvated species (clusters) of specific composition and size, as well as often-predictable structure. With regard to studying electron dynamics in diverse environments and interfacing gas- and condensed-phase chemistry, cluster anions are ideal model systems and platforms for the studies of microscopic solvation and elementary chemical processes in condensed environments.[27] In addition, negative ions are appealing experimentally because the excess electron can be photodetached in a much gentler way than in the case of photoionization of neutral molecules. The relatively low electron affinities of most neutrals enable electron photodetachment from anions by a single visible or UV photon, simplifying the experiment and its interpretation.

A particularly powerful variant of photoelectron imaging is its implementation in conjunction with ultrafast pump–probe techniques.[28–30] Femtosecond time-resolved photoelectron imaging is ideally suited for observing the electronic structure evolution in chemical reactions.[31] Chemical reaction can be induced by an abrupt change in the electronic structure (e.g. promotion of an electron from a bonding to an antibonding orbital). As such change sets the nuclei in motion, the electronic wavefunction itself begins to evolve, adapting adiabatically to the changing molecular geometry and responding to possible nonadiabatic couplings between states. Photoelectrons detached at various reaction stages exhibit different energy and angular distributions, resulting in time-dependent photoelectron images. These images, as signatures of the parent orbitals, reflect the evolving electronic structure of the reacting system. Hence, time-resolved photoelectron imaging can be used to sample a wide range of quantum processes, encompassing bond cleavage, nonadiabatic transitions, vibration, rotation, wave packet dynamics, and others.[32–56]

In the following section, we present a brief conceptual overview of the photoelectron imaging approach to anion photoelectron spectroscopy. In Section 3, the utility of photoelectron imaging in obtaining effective 'signatures' of the bound electron orbitals is discussed, alongside a qualitative symmetry-based overview of the image interpretation. Section 4 presents examples of microscopic solvation effects observed in the photoelectron imaging experiments on cluster anions, in which the solvent is bound to the anion core mainly by electrostatic interactions. These anion-neutral interactions are relatively weak compared to the covalent forces discussed elsewhere in this paper, but are nonetheless much stronger than the corresponding van der Waals interactions encountered in neutral clusters. Section 5 is devoted to the multi-centre view of negative-ion photodetachment, introducing a conceptual view of the diatomic and covalent dimer anions as 'static' molecular interferometers. This discussion lays the groundwork for the dynamic dual-centre interference effects in time-resolved photoelectron imaging of symmetric diatomic anion dissociation, discussed in Section 6. A portion of the same section is devoted also to the energetic perspective of the bond breaking, as seen in the time-resolved photoelectron imaging experiments.

2. The imaging approach

Photoelectron imaging is a powerful yet straightforward experimental technique for probing the electronic structure and its transformations in various contexts. Relating experimental observables to the underlying electronic structure, as described by the time-independent Schrödinger equation, other spectroscopic techniques have traditionally focused on transition frequencies, i.e. the intervals between the energy eigenvalues. Without sacrificing the energy-domain observables, imaging sheds light on other structural characteristics, the symmetry of electronic wavefunctions being one example.

The imaging technique, as applied to gas-phase reactions, was pioneered by Chandler and Houston in 1987 in the context of photofragment-ion imaging of neutral-molecule dissociation.[1,2] Many groups have since used imaging to measure scalar and vector correlations and energy partitioning in various contexts, including photodissociation,[2,57–62] reactive and inelastic collisions,[3,60,63–65] dissociative photodetachment and photofragment-photoelectron coincidence spectroscopy,[66–71] and others. With the introduction of velocity mapping in 1997,[16,17] the popularity of imaging experienced explosive growth,[2,3,18] and photoelectron imaging has become a widely used photoelectron spectroscopic technique. The resolution is either comparable to or exceeds that of other, traditional approaches. For example, a truly remarkable resolution of $\Delta E/E = 0.38\%$ was recently demonstrated by Cavanagh *et al.*,[25] enabling a detailed study of fine-structure transitions in atomic-anion photodetachment.

The conceptual approach, as it applies to anion photoelectron imaging, is illustrated in Figure 1 for the example of the photodetachment of CS_2^- using linearly polarized 800 nm light.[8] A packet of mass-selected anions is illuminated by a laser pulse between the electrodes of an electrostatic velocity-mapping lens. The resulting photoelectron cloud is then projected on a position-sensitive detector using an arrangement of electric fields. Mathematically speaking, the two-dimensional projection (image) contains all essential information about the original three-dimensional photoelectron distribution, provided the cylindrical symmetry axis, defined by the laser polarization direction, lies parallel to the

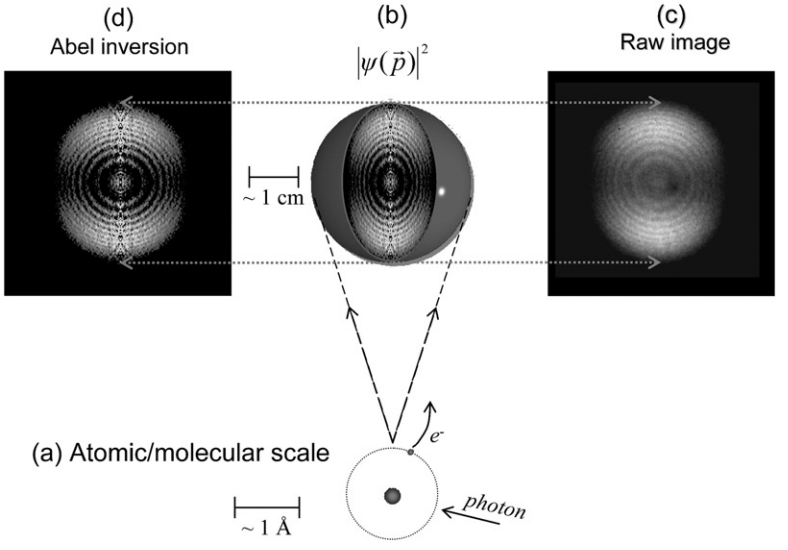

Figure 1. Schematic illustration of photoelectron imaging, using the 800 nm CS_2^- data. The laser polarization is assumed vertical in the figure plane. (a) The photodetachment from an individual anion occurs of a sub-nano (Angstrom) scale. (b) Schematic depiction (with a cut-away) of the photoelectron cloud, which has expanded to the macroscopic dimensions. The cloud consists of several concentric spheres, giving rise to rings in the photoelectron image, which in turn correspond to the vibrational progression in the photoelectron spectrum. (c) The raw photoelectron image – a projection of the three-dimensional cylindrically symmetric photoelectron cloud on a two-dimensional position sensitive imaging detector. (d) The Abel inversion reconstructed from the raw image in (c) using the BASEX method. The 'inverted' image represents a central slice through the cylindrically symmetric photoelectron cloud. It is also shown in the cut-away in (b).

detector plane.[2] Hence, we can consider the imaging process as a way of observing the nascent photoelectron cloud as if external fields were absent.

The expanding photoelectron cloud originates from a finite initial volume, determined by the overlap between the laser and ion beams. Hence the original imaging technique, which employed a parallel electric field to project the cloud onto the detector, suffered from a spatial blurring of the images, attributable to the finite initial volume.[2] The velocity-mapping arrangement of Eppink and Parker[16] minimizes this problem, eliminating (in the first order) the spatial smearing by effectively reducing the photoelectron source volume to (essentially) zero.

The number of photoelectrons varies from <0.1 to >100 per experimental cycle, while a quality image might include more than 10^5 electron impacts. Due to velocity mapping, we can view all these electrons as emitted simultaneously from a point source at $\vec{r}=0$. The laboratory-frame velocity vector distribution is determined by the photoelectron wavefunction, defined in terms of the nascent velocity or momentum: $\psi=\psi(\vec{p})$. In physical space, ψ corresponds to a wave emitted on an initially microscopic, molecular scale (Figure 1(a)). Non-relativistic electron momenta and positions within the unperturbed photoelectron cloud are related by $\vec{p}=m_e\vec{r}/t$, where t is time measured from the photodetachment event and m_e is the electron mass. In a few tens of nanoseconds the

cloud typically expands through many orders of magnitude, reaching the macroscopic dimensions that allow it to be imaged Figure 1(b), while retaining the nascent distribution in momentum space. At any time t, the photoelectron distribution can be mapped from the physical ($\vec{r}$) to momentum ($\vec{p}$) space and vice versa, using the above classical relation.

The act of measurement collapses the wavefunctions of individual electrons on eigenfunctions of the measurement operator. Imaging measures particle positions and the corresponding eigenfunctions are delta-functions of the coordinates. That is to say that individual electrons appear on the detector as localized spots, although an image resulting from many impacts represents a projection of the laboratory frame (LF) probability density $|\psi|^2$. Due to the cylindrical symmetry imposed by the light polarization, the original three-dimensional $|\psi|^2$ distribution can be uniquely reconstructed by an inverse integral transformation, known as Abel inversion.[2] The inversion yields a central slice (Figure 1(d)) through the three-dimensional cylindrically symmetric distribution, which can be viewed, equivalently, either in $\vec{p}$ or $\vec{r}$ space. The reconstruction procedure is a crucial part of data analysis; without it, photoelectron imaging would not be a quantitative spectroscopic technique. (Some novel experimental techniques, such as slice-imaging,[64,72–77] allow one to bypass the reconstruction requirement. However, these techniques are applicable mainly to photofragment-ion imaging; their application to photoelectrons remains challenging due to the much faster time-scales involved.) Although Abel inversion provides a unique solution to the reconstruction problem, it is extremely susceptible to experimental noise. Several approaches have been developed to address this problem mathematically.[2,78–81] Among them is the widely used BAsis Set EXpansion (BASEX) method,[78] which involves the expansion of experimental images in the basis set of analytical Abel-transformed functions.

From an Abel-inverted image, the corresponding photoelectron energy spectra and photoelectron angular distribution (PAD) can be determined. In a one-photon process involving linearly polarized light the PAD is generally described by the equation:[82]

$$I(\theta) = a[1 + \beta P_2(\cos\theta)], \tag{1}$$

where θ is the angle between the photoelectron velocity vector and the light's electric field vector (i.e. the laser polarization direction), $I(\theta)$ is the probability of electron emission at a particular angle θ, a is a normalization constant proportional to the total photodetachment cross-section, $P_2(\cos\theta)$ is the second-order Legendre polynomial, and β (ranging from -1 for purely perpendicular transitions to $+2$ for purely parallel transition) is commonly termed the anisotropy parameter. The β parameter fully characterizes a one-photon PAD and provides the most direct experimental indication of the character of the photodetachment process and the nature of the parent bound orbital, from which the photodetached electrons originate.

In a two-photon (for example, pump–probe) process, the PAD is generally described by the higher-order equation:

$$I(\theta) = a[1 + \beta_2 P_2(\cos\theta) + \beta_4 P_4(\cos\theta)], \tag{2}$$

which includes an additional, fourth-order Legendre polynomial and the corresponding expansion coefficient, β_4.

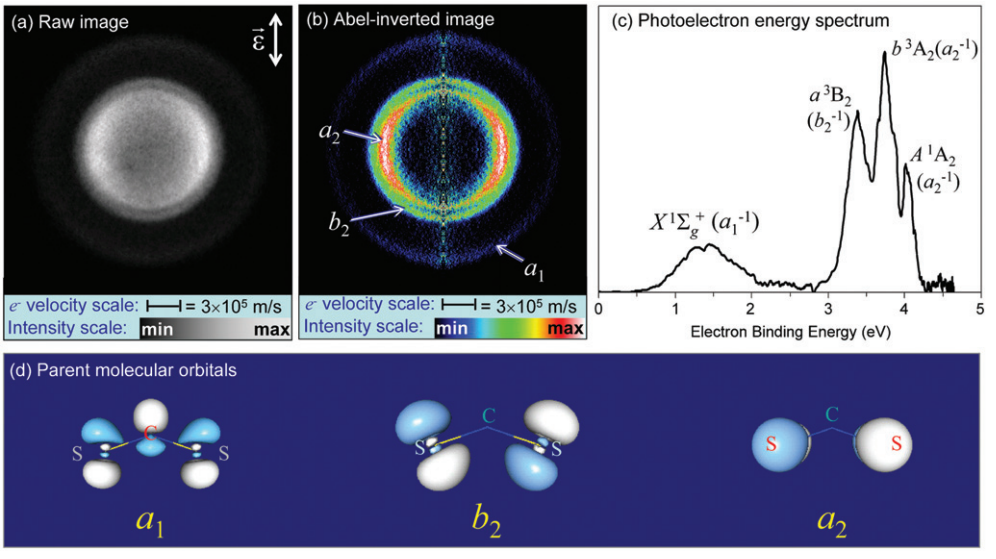

Figure 2. Photodetachment imaging of CS_2^-. (a) The raw photoelectron image as it was obtained in the experiment with linearly polarized 267 nm laser radiation integrating over 30,000 laser pulses. (b) The Abel-inverted (reconstructed) image obtained from the raw image in (a), presented here using a colour intensity scale for clarity. (c) The corresponding photoelectron spectrum, showing transitions to several electronic states on the neutral molecule. Symbols in parentheses indicate the anion orbitals from which the electrons are ejected under the single-electron approximation. (d) The molecular orbitals involved in the photodetachment. The corresponding bands in the photoelectron image (i.e. the orbital 'signatures') are indicated by arrows in (b).

3. Electronic structure of negative ions via photoelectron imaging

The electronic structure of stable molecules and ions is described with reasonable accuracy (in most cases) within the Born–Oppenheimer approximation and the molecular orbital (MO) theory. The use of photoelectron imaging for obtaining 'signatures' of the bound electron orbitals is fundamental to many applications of the technique. In recent years, many groups have used photoelectron imaging to characterize the electronic structure of molecular anions, with some examples found in Refs.[11,19–24]

As a specific illustration, Figure 2 displays the results of a photoelectron imaging study of CS_2^- photodetachment.[9] The photoelectron projection in Figure 2(a) was recorded with 267 nm light polarized vertically in the image plane. The Abel inversion obtained using the BASEX algorithm[78] is shown on a colour scale (for extra clarity) in Figure 2(b). The perceptible vertical line through the centre on the reconstructed image is caused by experimental noise, amplified by the inversion procedure, and marks the cylindrical symmetry axis of the 3-D distribution. The experiment reveals distinct photoelectron bands, seen as three concentric rings, which are particularly clear in the reconstructed version of the image in Figure 2(b). The photoelectron spectrum presented in Figure 2(c) contains four identifiable transitions, marked in accordance with the assignment of the corresponding neutral electronic states. (The four spectral peaks arise from only three perceptible rings in the image, because the A^1A_2 band appears as an inner shadow of the intense $b\,^3A_2$ ring.)

Within the one-electron, molecular-orbital description of the photodetachment process, these spectral bands image rings correspond to electron detachment from three different molecular orbitals of CS_2^-: the singly-populated a_1 HOMO, and the doubly-occupied b_2 (HOMO-1) and a_2 (HOMO-2) orbitals. Isosurface sketches of these orbitals are shown in Figure 2(d), while the rings in the Abel-inverted image in Figure 2(b) are labeled in accordance with the orbitals they represent. As mentioned above, the a_2^{-1} band consists of two spin-components, corresponding to the $b^3A_2 \leftarrow X^2A_1$ and $A^1A_2 \leftarrow X^2A_1$ transitions, which involve the removal of the $\downarrow$ and $\uparrow$ electrons from the a_2 orbital, respectively. In principle, b_2^{-1} photodetachment can also yield both the $^3B_2$ and $^1B_2$ neutral states; however, the singlet is not accessible at the 267 nm photon energy.[83]

The a_1, b_2, and a_2 rings in the photoelectron image display markedly different angular distributions with respect to the laser polarization axis (see Ref.[9] for quantitative analysis), reflecting the differing symmetry properties of the corresponding bound orbitals. For example, the PAD of the $X^1A_1 \leftarrow X^2A_1$ transition, peaking in the laser polarization direction, is characteristic of detachment from a totally symmetric orbital, which results in a parallel photodetachment transition with $\beta > 0$.[8,9] The quantitative modeling of angular distributions requires accounting for interference between multiple detachment channels and complex phase interactions,[82,84–91] which can be particularly unintuitive in a molecular-anion case. However, physical insights can be gained from much simpler qualitative models. One such symmetry-based approach, dubbed the *s*&*p* model, has been illustrated for several molecular anions, including CS_2^-.[8,9] It establishes a qualitative relationship between the photoelectron angular distributions and the symmetry properties of the corresponding parent orbital.

The wavefunction of a free (photodetached) electron can be expanded in terms of partial waves with definite values of orbital angular momentum. For example, an electron detached from an atomic *p* orbital produces *s* and *d* waves, in accordance with the selection rule $\Delta\ell = \pm 1$. Molecular orbitals, in general, cannot be assigned single ℓ values. However, one can apply group theory and dipole selection rules to determine the symmetry of the free electron wavefunction (ψ_f) and then have it expanded in the symmetry-adapted basis of partial waves with definite ℓ values.[92] An additional complication arising in the molecular-anion case is the need to consider all possible orientations of the parent anions in the LF.

The *s*&*p* model, applied to molecular anions, first considers the detachment in the molecular frame (MF), requiring that the direct product of the irreducible representations of ψ_f, the dipole operator ($\hat{\mu}$), and the initial bound orbital (ψ_{MO}) is invariant under the symmetry operations of the molecular point group. After determining the allowed symmetries of the free-electron waves, ψ_f can be expanded in a basis of partial waves with defined ℓ values, emitted from a single centre. The model then makes a further approximation, limiting the consideration only to the partial waves with $\ell \leq 1$. This approximation relies on the effective centrifugal suppression of the higher-order free-electron waves in negative-ion photodetachment – the same effect that gives rise to the Wigner threshold law.[93] However, while the Wigner law holds strictly only in the immediate proximity of the photodetachment threshold,[94] the effective suppression of the higher-ℓ waves relative to the smaller-ℓ waves is felt over a broader energy range. Therefore, although the above $\ell \leq 1$ approximation is best justified for slow electrons, we see it as a reasonable qualitative assumption for eKEs of up to (typically) a few electron-volts.

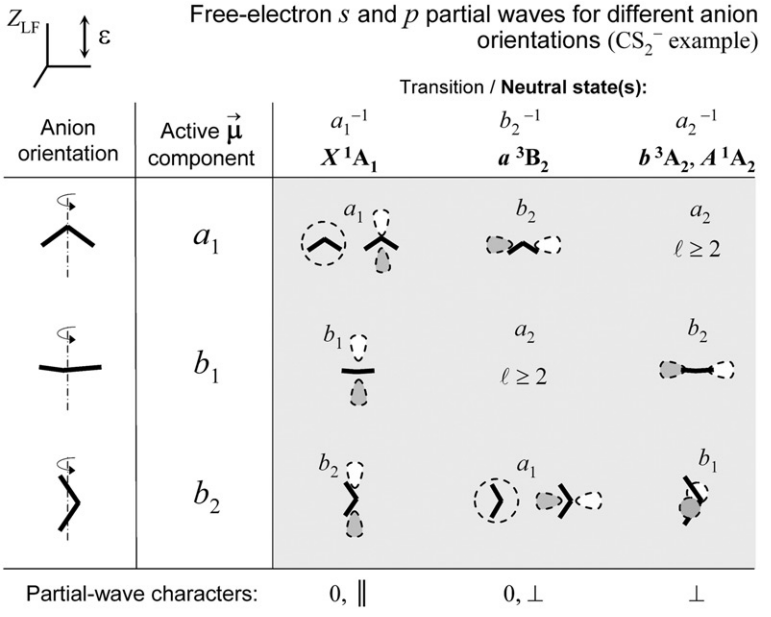

Figure 3. The *s&p* model treatment of CS_2^- photodetachment. First column: principal anion orientations, with the solid line representing the bent frame of CS_2^-. Second column: symmetries of the transition-dipole components driven by the laser radiation polarized along the LF *z*-axis, corresponding to the principal orientations. The shaded area in the table indicates the symmetries and *s* and *p* components (shown as dash contours) of ψ_f corresponding to the respective transitions and principal orientations. See the text for details.

Next, the emitted *s* and *p* waves considered by the model must be referenced from the MF to the LF axes. In general, the LF PAD is determined by integrating over all molecular orientations, accounting for the proportionality of transition amplitudes to the cosine of the angle between the transition dipole (defined in the MF) and the LF-based laser polarization axis. In the *s&p* approach, the PAD's qualitative nature is determined by considering only few 'principal' orientations of the anion. This substitute for orientation averaging is, of course, another coarse approximation, designed to give a conceptual picture of the detachment process without embarking on complete quantum calculations.

We will now outline the application of the *s&p* model to the benchmark case of CS_2^-, making use of the symmetry elements of the C_{2v} point group to which this anion belongs. The chosen 'principal' orientations of CS_2^- correspond to one of the molecular axes aligned along the laser polarization direction, i.e. the LF *z* axis (z_{LF}), as shown schematically in the left column of Figure 3. For each orientation, only the transitions with non-zero dipole components along z_{LF} are active. The symmetry species of the active dipole components are indicated in the second column in Figure 3. These species are the irreducible representations of z_{LF} in the MF for the corresponding anion orientations. Since only the irreducible representation of the dipole component along z_{LF} is important in the following discussion, all conclusions remain valid if the molecule is rotated about z_{LF}, as indicated in Figure 3, or inverted in the plane perpendicular to z_{LF}. The three shaded columns in Figure 3 list the orientation-dependent symmetries of the free electron, determined in the

MF by requiring $\langle\psi_f|\hat{\mu}|\psi_{MO}\rangle \neq 0$ for the indicated photodetachment transitions. For example, for b_2^{-1} the free electrons emitted from the anion orientations corresponding to the a_1, b_1, and b_2 active dipole components are of b_2, a_2, and a_1 symmetries, respectively.

Invoking the *s&p* model, ψ_f is expanded in a single-centre basis of partial waves with definite ℓ values, limiting the consideration to *s* and *p* partial waves only. An *s* wave always corresponds to the totally symmetric representation (a_1 in the C_{2v} point group case), but *p* waves can transform as a_1, b_1, or b_2 C_{2v} symmetry species, depending on their polarization in the MF. The dashed contours in Figure 3 show schematically the allowed *s* and *p* components of ψ_f under the symmetry constraints determined above. For free-electron waves transforming as a_1 (e.g. a_1^{-1} detachment from the first principal orientation in Figure 3 and b_2^{-1} detachment from the third orientation), both *s* and *p* components are allowed. While the *s* waves are isotropic, the LF polarization of the *p* waves is determined by their MF symmetry and the corresponding anion orientation. For b_1 and b_2 waves, only *p* components are allowed in the *s&p* model. For a_2 waves, the smallest-ℓ components correspond to *d* partial waves; therefore, a_2 waves are neglected completely under the $\ell \leq 1$ approximation.

Considering the wave sketches in the shaded area of Figure 3, the qualitative nature of the expected PADs becomes clear. For the a_1^{-1} ($X^1A_1 \leftarrow X^2A_1$) transition, the free-electron wavefunction is characterized by interference of isotropic *s* waves ('0' anisotropy character) and *p* waves polarized along z_{LF} ('$\parallel$' character). Thus, a PAD with positive β is expected, in agreement with the experimental results in Figure 2. The *s&p* model prediction of the nature of a_1^{-1} PAD holds at other detachment wavelengths. For example, the 800 nm PAD for the $X^1A_1 \leftarrow X^2A_1$ transition integrated over all eKEs is characterized by $\beta = 0.68$ (see Figure 1) and similar values were also obtained at 530 and 400 nm.[8,9] For the b_2^{-1} ($a\ ^3B_2 \leftarrow X\ ^2A_1$) transition, the model predicts two principal *p* waves with amplitudes peaking perpendicular to the laser polarization ('$\perp$' character), as well as an isotropic ('0' character) *s* wave. Thus, $\beta < 0$ is expected, as is indeed observed in the experiment (see Figure 2). For the a_2^{-1} ($b\ ^3A_2$, $A\ ^1A_2 \leftarrow X\ ^2A_1$) transition, $\ell = 0$ components of ψ_f are forbidden under the electric-dipole approximation and only horizontally polarized ('$\perp$' character) *p* waves are produced in the detachment under the *s&p* model approximations. A substantially negative value of β is therefore predicted for b_2^{-1} photodetachment.

For the b_2^{-1} and a_2^{-1} transitions above, negative values of the anisotropy parameter are predicted by the model. However, in the latter case, only *p* waves polarized perpendicular to z_{LF} are predicted for the principal orientations within the approximations of the model, while for the b_2^{-1} transition similar *p* waves are predicted to compete with an *s* component (which can be particularly intense for slow electrons). Another qualitative prediction can be drawn from these arguments: the perpendicular nature of the anisotropy is expected to be more pronounced in the pure *p* case (a_2^{-1} transition) than in the mixed *s* and *p* case (b_2^{-1}). That this prediction is also confirmed by the experiment is easily seen in the photoelectron image and its Abel transform in Figures 2(a) and (b): the a_2^{-1} transition does indeed exhibit a more negative anisotropy ($\beta = -0.44$ and -0.42 for $b\ ^3A_2$ and $A\ ^1A_2$, respectively) than the b_2^{-1} transition ($\beta = -0.24$ for $a\ ^3B_2$).

The above application of the *s&p* model to CS_2^- photodetachment makes use of the specific properties of the C_{2v} point group. The same general approach has been applied to

other molecular anions, such as, for example, O_2^-,[95] S_2^-,[9] NO^-,[96] and others.[22] In the particular cases of homonuclear diatomics, the model has been compared to the Cooper–Zare method[82,88,97] adapted to molecular anions[9] To this end, we note that the *s*&*p* model offers a pedagogical advantage of the ease of visualization, as long as the photodetachment is considered in a qualitative manner only.

4. Solvation interactions via photoelectron imaging

The excess electron orbitals in negative ions tend to be diffuse, making them particularly sensitive to external perturbations and intermolecular interactions. As photoelectron imaging is sensitive to the structure of bound electron wavefunctions, it presents a valuable tool for studying electrostatic and covalent interactions in the gas-phase cluster-anion context.[5,8,23,24,98–109]

The solvation effects on the anion electronic structure and photodetachment dynamics are illustrated here on the example of solvated iodide cluster anions. The photoelectron images and corresponding spectra shown in Figure 4 represent a study of the $I^-\cdot Ar$, $I^-\cdot H_2O$, and $I^-\cdot CH_3I$ cluster anions in comparison with bare I^-.[108] Although in all these cases the excess electron is localized predominantly on the I^- cluster core, even casual visual inspection of the images reveals differences between them. These differences can only be explained by the presence of respective solvent species and are, therefore,

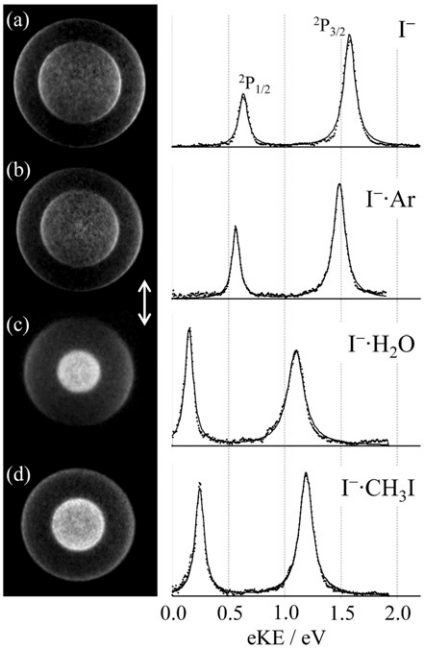

Figure 4. Solvation effects in photoelectron imaging. Shown are the photoelectron images and corresponding spectra obtained in 267 nm detachment of (a) I^-, (b) $I^-\cdot Ar$, (c) $I^-\cdot H_2O$ and (d) $I^-\cdot CH_3I$. The detachment laser is polarized vertically in the image plane, as indicated by the white double-arrow.

attributed to solvation interactions. For example, the photoelectron images observed for I^- solvated by H_2O or CH_3I, seen in Figures 4(c) and (d), respectively, are qualitatively different from the bare I^- image in Figure 4(a). At the same time, the I^- and $I^-\cdot Ar$ images in Figures 4(a) and (b), respectively, are quite similar, signaling a weak interaction of the inert Ar atom with I^-.

In all four images/spectra presented in Figure 4, features are observed correlating to two photodetachment channels, which yield neutral iodine atoms in the ground $^2P_{3/2}$ and excited $^2P_{1/2}$ spin–orbit states, respectively. In the photodetachment of I^- and $I^-\cdot Ar$, the branching ratio of the $^2P_{1/2}$ and $^2P_{3/2}$ channels is approximately 0.4, falling short of the statistical ratio of 0.5. This non-statistical behaviour is explained by the relative suppression of the lower-eKE $^2P_{1/2}$ channel due to the Wigner-type effect of the centrifugal barrier in anion photodetachment.[93,110] In contrast, for both $I^-\cdot H_2O$ and $I^-\cdot CH_3I$ the $^2P_{1/2}$ to $^2P_{3/2}$ channel branching ratio increases by a factor of 1.6 compared to the bare iodide case, with the relative yield of the excited spin–orbit channel now exceeding the statistical expectation. The enhancement of the $^2P_{1/2}$ channel in the presence of polar solvent molecules was attributed to dipolar effects increasing the amplitude of the final-state continuum wavefunction in the vicinity of the neutral core, thus improving its overlap with the initial bound anion state.[108,111]

The angular distributions in the photodetachment of I^-, $I^-\cdot Ar$ and $I^-\cdot H_2O$ are understood within the framework of direct photodetachment from a $5p$ atomic orbital of the I^- core. The PADs are described well by the Cooper–Zare central-potential model.[82,88,97] whereas the solvation in the cluster systems affects mainly the eKE used to calculate the anisotropy values. In contrast, the nearly isotropic angular distributions in both $I^-\cdot CH_3I$ photodetachment channels deviate sharply from the Cooper–Zare model predictions. This behaviour invokes alternative mechanisms, ascribing the solvent an active role in the electron emission process. The possible mechanisms include: photoelectron-solvent scattering; photoinduced electron transfer to the solvent followed by rapid autodetachment; CH_3I photodissociation followed by a bimolecular reaction of CH_3 and I^- yielding an autodetaching CH_3I^- product.[108] In view of the latest electron-solvent scattering results for other cluster-anion systems,[96] the scattering mechanism, involving short-lived solvent anionic resonances, appears to be the most plausible explanation of the above behaviour in $I^-\cdot CH_3I$.

In addition to the simultaneous measurement of photoelectron spectra and angular distributions, photoelectron imaging affords another important experimental advantage, particularly valuable in cluster studies: the uniform sensitivity to both fast and slow photoelectrons, all the way to $eKE = 0$. In experiments by several research groups, this feature of imaging revealed the prevalence of indirect detachment processes in cluster anions, which result in relatively slow (often described as thermal) and isotropic photoelectron distributions.[5–7,98,103,105,109,112,113] Underscoring the importance of indirect pathways, the predominance of autodetachment over direct photodetachment was revealed in several cluster types, such as for example $CO_2^-\ (H_2O)_n$, $n \geq 4$ at 400 nm.[109]

The observation of laser-induced autodetachment highlights the *presence* of low-lying excited electronic states of the cluster anions studied. These states are crucial for understanding cluster reactivity – particularly so, if they arise from covalent interactions between monomer constituents.[106,114–116] This proved to be the case, for example, for the dimer-anion-based $(OCS)_n^-$ clusters.[103,105] Unfortunately, apart from their existence,

'static' (one-photon) photoelectron imaging alone reveals little about the *nature* of the autodetaching excited states, often due to the 'thermal' (featureless) and isotropic nature of the resulting photoelectron distributions. However, recent work has shown that a combination of photoelectron imaging with photofragment spectroscopy,[109,117,118] targeting both the electron-emission and nuclear-rearrangement pathways involved in the excited-state decay, provides an effective tool for deciphering these aspects of cluster-anion dynamics and reactivity. Yet even more detailed insights into the excited-state relaxation processes are provided by time-resolved photoelectron imaging,[71,119,120] pioneered (in the negative-ion context[10,29]) by the Neumark group.[12,14,99,100,113]

5. A multi-centre view of photodetachment: Diatomic and dimer anions as 'static' molecular interferometers

In Section 3 we described a symmetry-based approach to understanding photoelectron angular distributions, which relies, essentially, on the character tables of relevant point groups. In the following we consider the effects of a different type of symmetry encountered in systems consisting of two (or, in principle, more) equivalent atoms or moieties. Such equivalency usually implies a high level of molecular symmetry, but there is a significant degree of flexibility with regard to the specific symmetry operations and symmetry point groups involved. In the examples reviewed in this paper, we will encounter homonuclear diatomics ($D_{\infty h}$ point group) and polyatomic anions belonging to the C_{2v}, D_{2d}, and possibly D_{2h} point groups. The specific representations are less important than the fact that the detachment of an excess electron, initially shared (equally) between two identical atoms or moieties, can be viewed as superposition of two *equivalent* and *indistinguishable* emission centres. Such effects are relevant to the photodetachment of homonuclear diatomics and dimer anions with delocalized charge distributions. Similar considerations apply to the photoionization of neural diatomics and dimer molecules.

The phenomenon of dual- (or multi-) centre interference in photodetachment is intimately related to other well-known quantum effects, such as, for example, the classic double-slit experiment[121] and the interference between reaction channels giving rise to spectral Fano profiles.[122] Most relevant to the context of the present article, Cohen and Fano considered the ionization of electrons within a multi-centre molecular field by regarding the two atoms of a homonuclear diatomic as independent sources of photoelectrons.[123] Photoelectron imaging provides new demonstrations of the resulting interference phenomena, shedding light not only on the quantum properties of the electrons, but also the underlying electronic structure of static and dynamic anionic systems.

5.1. *The homonuclear diatomic anion*

A straightforward example of dual-centre interference is seen in the photodetachment of O_2^-, where the excess electron occupies a $2p\pi_g$* orbital shared between the two oxygen atoms. While the photodetachment of superoxide has been the subject of numerous experimental and theoretical studies, Figure 5(a) shows a 780 nm photoelectron image by Akin *et al.*[95] Only one half of the raw image is shown (in grey scale on the left), next to the matching half of the Abel inversion (in false colour on the right). The rings in the image

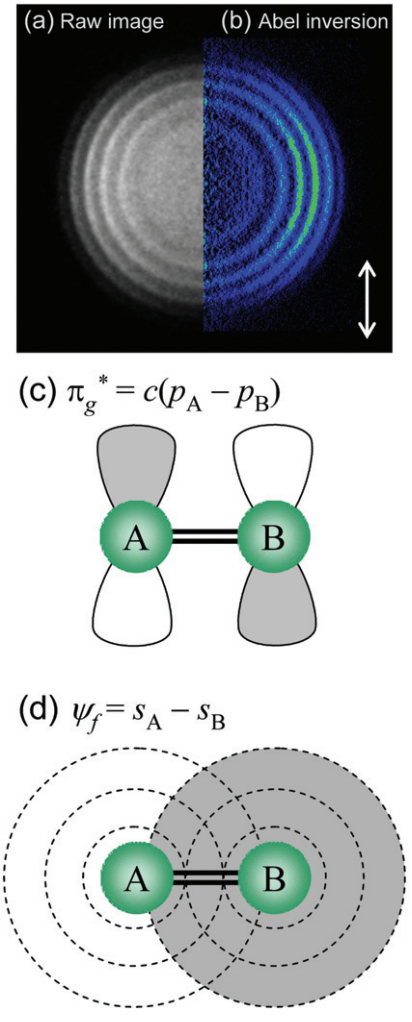

Figure 5. Photoelectron imaging of the superoxide anion. (a) and (b) are the raw and Abel-inverted images of O_2^- obtained at 780 nm. The detachment laser is polarized vertically in the image plane, as indicated by the double-arrow. (c) A schematic depiction of the O_2^- HOMO. (d) Opposite-phase *s* partial waves emitted from the two equivalent centres in O_2^- photodetachment.

correspond the $v' = 0\text{–}5 \leftarrow v'' = 0$ vibrational progression of the $O_2(X^3\Sigma_g^-) \leftarrow O_2^-$ $(X\,^2\Pi_g)$ photodetachment transition. The quantitative details of the image and spectral analysis are found elsewhere.[95] Here we focus exclusively on the qualitative aspects of photoelectron anisotropy, namely, its overall perpendicular (i.e. $\beta < 0$) character, which can be understood in several conceptual ways.

First, the PAD peaking in the equatorial direction perpendicular to the laser polarization is consistent with the *d*-like character[92] of the $2p\pi_g^*$ O_2^- HOMO, pictured schematically in Figure 5(b). As shown elsewhere,[95] the anisotropy parameter (β) values for different vibrational rings in Figure 5(a) are indeed described very well by the

Cooper–Zare central potential model, assuming $\ell = 2$ for effective orbital angular momentum of the initial orbital.

Second, it is possible to apply a symmetry-based *s*&*p* model approach to O_2^- photodetachment, similar to the formalism described in Section 3 on the example of CS_2^-. The detailed application of this approach to the case of π_g^{-1} photodetachment is described in Ref.[9] on the example of S_2^-. In short, under the *s*&*p* model approximations, only *p* partial waves polarized perpendicular to the laser polarization direction are emitted from any principal orientation in photodetachment from the $2p\pi_g$* HOMO of $O_2{}^-$. These waves result in a negative ($\beta < 0$) character of photoelectron anisotropy, consistent with the experimental observations in Figure 5 and the Cooper–Zare model.

The third, equivalent approach treats O_2^- as a two-centre interferometer. As seen in Figure 5(b), LCAO-MO theory describes the parent $2p\pi_g$* orbital as a superposition of $2p$ orbitals belonging to the two oxygen atoms, A and B: $\pi_g^* = c(p_A - p_B)$. The negative sign accounts for the antibonding, *gerade* character of the MO, while c is a normalization constant. As the initial state is a sum of two separated atomic states, the photoelectron can also be treated as a superposition of waves emitted from centres A and B, separated by the length of the O_2^- bond, i.e. $R \approx 1.2$ Å. According to the electric-dipole selection rule, each centre (i.e. the p_A and p_B atomic orbitals) emits *s* and *d* partial waves. In keeping with the assumptions of the *s*&*p* model (for simplicity and with the Wigner law in mind), we will disregard the *d* waves. The photodetachment process is thus approximated by a superposition of isotropic waves s_A and s_B, illustrated in Figure 5(c). These waves are emitted with equal amplitudes and opposite phases, accounting for the negative sign in the LCAO-MO expansion of the parent MO. Since de Broglie wavelength of the emitted electrons ($\lambda_e \sim 10$ Å) is significantly longer than R, s_A and s_B wave interference results in an effective *p*-like wave polarized along the O_2^- internuclear axis. This free-electron wave has a node in the mirror symmetry plane perpendicular to the molecular bond, where the opposite-phase contributions of s_A and s_B cancel each other out exactly. It remains to note that the individual $p_A \rightarrow s_A$ and $p_B \rightarrow s_B$ transition are maximized when the p_A and p_B axes are parallel to the laser polarization direction, which happens for the O_2^- ions aligned perpendicular to the laser polarization axis. Hence the most intense free *p*-like electron waves are emitted in the direction perpendicular to the laser polarization, giving rise to the negative anisotropy character observed in the photoelectron image in Figure 5.

The above three conceptual descriptions of photodetachment are consistent with each other and yet one may justifiably argue that the *qualitative* *s*&*p* and two-centre interferometer approaches do not provide extra physical insight that cannot be gained from the *quantitative* Copper–Zare central-potential model. This may indeed be the case for the rather straightforward case of O_2^-. It is argued, however, that the predictive power of both the *s*&*p* and the dual-centre descriptions becomes invaluable in more complex molecular and cluster systems, to which the central-potential model is not even approximately appropriate.

5.2. *Covalent dimer anions*

The interferometer approach, in particular, simplifies the description of molecular structures with delocalized electron orbitals, such as covalently bound dimer anions. In several important and well-known cases, such as the $(CO_2)_2^-$, $(OCS)_2^-$, and $(CS_2)_2^-$

dimer-anion family, the dimer HOMO can be conveniently thought of as a superposition of two monomeric orbitals. The detachment from the dimer anion can then be described in terms of the interference of electron waves originating from the two monomeric moieties. Note that inversion symmetry (present in the O_2^- case) is not required. The only necessary symmetry is the existence of two *equivalent* monomeric moieties, such as, for example, in the covalent $(OCS)_2^-$ dimer anion, which has a C_{2v} symmetry equilibrium structure.[116,124]

Covalent dimer anions, in general, and the competition/coexistence of different electronic and structural cluster-anion isomers, in particular, have attracted considerable attention. One extensively studied effect of competition between the covalent and solvation interactions in anionic cluster environments is core switching in the $(CO_2)_n^-$ cluster anions. Specifically, the clusters with $2 \leq n \leq 6$ and $n \geq 14$ contain the covalently bound $(CO_2)_2^-$ (i.e. $C_2O_4^-$) cluster cores, while in the intermediate size range ($6 < n < 14$), the CO_2^- based clusters are present.[125–127] Since the covalent $(CO_2)_2^-$ dimer-anion and the monomer CO_2^- anion are different chemical species,[114] *a priori* it would be only natural to expect that photoelectron imaging experiments on $(CO_2)_n^-$ should yield easily distinguishable signatures of the $CO_2^-(CO_2)_{n-1}$ and $(CO_2)_2^-(CO_2)_{n-2}$ clusters, particularly in the form of the angular distributions, which are claimed to reflect the parent orbital structure.

Yet the experiment yielded intriguing similarity of the PADs obtained from the monomer and covalent-dimer based $(CO_2)_n^-$ clusters.[106,107,109] For example, Figure 6 displays the values of the anisotropy parameter determined for representative monomer and dimer based $(CO_2)_n^-$ cluster anions studied at 400 nm, plotted for consistency as functions of eKE.[106] Details of the analysis are found in an earlier publication;[106] here we merely note that there is no significant quantitative difference betweens the PADs originating from the monomer and dimer-anion cores of the $(CO_2)_n^-$ clusters.

The dual-centre interference approach helps understand these results. Using the Linear Combination of Molecular Orbitals (LCMO) approximation,[128] the HOMO of the covalent dimer-anion $(CO_2)_2^-$ is thought of as a superposition of two monomeric orbitals: $\psi_{\text{dimer}} \approx c(\psi_A + \psi_B)$, as illustrated schematically in the inset in Figure 6. Here,

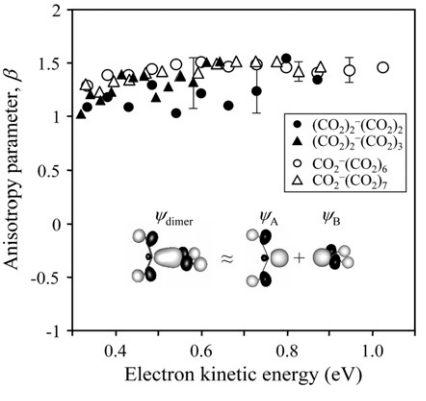

Figure 6. Energy dependence of the photoelectron anisotropy for representative monomer-based (open symbols) and dimer-based (filled symbols) $(CO_2)_n^-$ cluster anions. The error bars reflect one standard deviation in the data. The inset shows a sketch of the dimer-anion HOMO and its decomposition into the corresponding monomeric orbitals under the LCMO approximation.

ψ_A and ψ_B are each the LUMOs of the corresponding neutral CO_2 moieties (bent out of their linear equilibrium geomeries to accommodate the charge). Equivalently, ψ_A and ψ_B can be viewed as HOMOs of the CO_2^- monomer anions, although in the superposition state these monomeric orbitals are each populated effectively with 1/2 electron only, corresponding to a $^{-1/2}(O_2C)$–$(CO_2)^{-1/2}$ dimer-anion structure[114] The detachment from ψ_{dimer} is then a sum of waves originating from the two CO_2 moieties. This correlation enables a direct comparison of the $(CO_2)_2^-$ and CO_2^- PADs. Since the distance between the two moieties ($R \sim 2$ Å) is significantly shorter than the de Broglie wavelength of the photoelectrons ($\lambda_e \approx 15$ Å, corresponding to eKE = 0.7 eV), the two wave sources appear almost overlapped. Assuming zero initial phase-shift, the overall wave from the dimer anion will then appear similar to that from just one source (a monomer), yielding a similar PAD.

An even more interesting perspective is derived from comparison of the $(CO_2)_n^-$ results to those for $(CS_2)_n^-$. The $CS_2^-(CS_2)_{n-1}$ and $(CS_2)_2^-(CS_2)_{n-2}$ clusters do indeed yield qualitatively different PADs depending on their core structures.[104,106,129] These observations are reconciled with the LCMO and dual-centre interference picture by considering the qualitatively different electronic structures of the covalent dimer anions of CS_2 and CO_2. Although the structure of $(CS_2)_2^-$ is not yet fully understood,[83,106,115,129,130] it is clear that unlike $(CO_2)_2^-$, its HOMO is not a superposition of the a_1 HOMOs of two CS_2^- monomers. Instead, it is formed by overlap of lower-lying monomeric orbitals and therefore different PADs are expected in the detachment from the CS_2^- and $(CS_2)_2^-$ HOMOs.[106]

6. Time-resolved photoelectron imaging of bond dissociation

Photoelectron imaging in combination with femtosecond pump–probe techniques,[131,132] allows observation of chemical reactions on the natural time-scale of atomic rearrangements,[133] while emphasizing the electronic-structure perspective. In recent years, time-resolved photoelectron imaging studies have been employed to examine the electron transfer and relaxation dynamics in molecular cluster anions,[12,14,99,100,113] to observe the electronic-structure evolution from activated reactants to final products in molecular-anion dissociation,[10,134–136] to test theoretically calculated anionic potentials,[135,137] and to characterize coherence and symmetry-related interference effects in electron emission from electronically excited molecular systems.[10,15,136] In this Section, we focus on the characterization of excited-state potentials and manifestations of dynamic dual-centre interference in time-resolved photoelectron imaging experiments.

6.1. *Imaging of the reaction coordinate*

The I_2^- anion has been a benchmark system in the development of time-resolved photoelectron spectroscopy of negative ions, beginning with the pioneering work of Neumark and coworkers.[10,29,131] The evolution of time-resolved photoelectron spectra in the experiments by both the Neumark[10,131,137] and Sanov[135,136] groups indicated that the dissociation on the excited $A'\ ^2\Pi_{g,1/2}$ state of I_2^- induced with 780–800 nm femtosecond laser pulses is complete in < 1 ps. Figure 7(a, left) shows the relevant potential energy

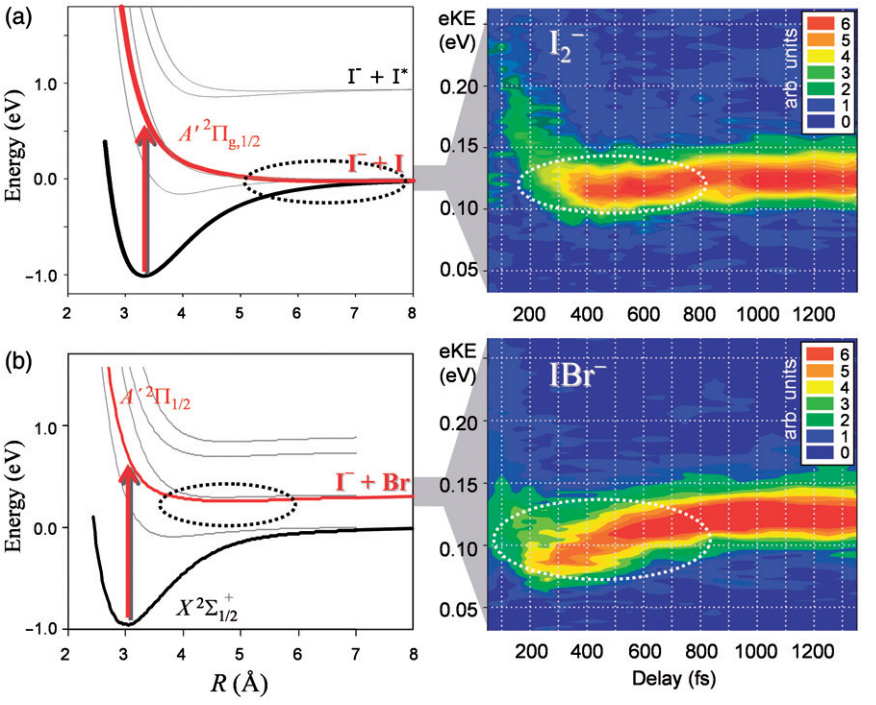

Figure 7. (a) The diagram on the left shows the potential energy curves of I_2^-, with the vertical arrow indicating a 780 nm pump launching the dissociation on the A' excited state. The time–energy plot on the right displays the evolution of the photoelectron spectrum throughout the dissociation process, as probed via photoelectron imaging with 390 nm probe laser pulses. (b) The same for IBr^-. Note that the relationship between R in the potential energy diagrams on the left and the time axis on the right is not quite linear.

curves of I_2^-, with the vertical arrow indicating a 780 nm pump launching the dissociation on the A' excited state, whose potential is shown in red. The time–energy plot on the right, $I(\mathrm{eKE}, t)$, displays the evolution of the photoelectron spectrum throughout the dissociation process, as probed via photoelectron imaging with 390 nm probe laser pulses. These results by Mabbs *et al.*[135] are in agreement with the earlier findings by Neumark and coworkers.[131,137]

The time–energy plot in Figure 7(a, right) displays a single photoelectron band, which asymptotically (at long delays) corresponds to the $I(^2P_{3/2}) \leftarrow I^-$ photodetachment (probe) transition. At short pump–probe delays, the band's maximum gradually shifts towards smaller eKE with increasing pump–probe delay, while its width narrows. The initial narrowing of the band reflects the transition from the molecular to atomic character of the initial bound orbital, from which the photoelectrons are emitted. Similar narrowing trends were also seen in other systems, for example, in the I^- channel of I_2Br^- photodissociation at 388 nm studied by time-resolved photoelectron imaging with the same-colour probe.[134] The decrease in peak eKE at short delays in Figure 7(a, right) is followed by a slight reverse shift to larger eKE, and by about 800 fs all perceptible spectral variations cease. The contour plot in Figure 7(a, right) reflects the approximate shape of the A' potential,

since pump–probe delay t can be converted (semi-classically) to internuclear distance R via the dissociation trajectory $R(t)$.[135] In particular, the transient eKE dip, circled with a dashed white line in Figure 7(a, right), corresponds to a barely perceptible well on the A' potential, also indicated with a circle on the potential energy diagram in Figure 7(a, left). The well arises from a long-range polarization-induced attraction between the $I(^2P_{3/2}) + I^-$ fragments, giving rise to a shallow (0.017 ± 0.010 eV) potential minimum at $R \approx 6.2$ Å, as characterized by Zanni *et al.*[137]

The sensitivity of time-resolved photoelectron imaging to excited-state potential details is illustrated further by comparison of the benchmark I_2^- results to new findings from a photoelectron imaging experiment on IBr^-, displayed in Figure 7(b). The time-resolved photoelectron spectrum on the right represents the first such measurement on this anion and its results have been used for testing the recently calculated[138] IBr^- potential energy curves. As seen by comparing the potential energy curves in Figures 7(a) and (b), the $A'\ ^2\Pi_{1/2}$ state of IBr^- is also predicted to have a well, but compared to I_2^- the A' well in IBr^- is deeper (~0.06 eV) and located at a shorter internuclear distance. These differences stand out clearly in the comparison of the experimental time–energy plots for I_2^- and IBr^- in Figures 7(a) and (b), respectively. Indeed, the transient eKE dip in the IBr^- experiment, circled in Figures 7(b, right), measures ~50 meV, which is a visibly greater shift than in I_2^-. It also occurs at shorter delays, than the I_2^- dip. Based on the classical trajectories, modeling the IBr^- and I_2^- dissociation, these shorter delays correspond to smaller I–Br internuclear distance, compared to R at which the I_2^- well is found.

Further (quantitative) analysis is found elsewhere.[135] It includes the classical trajectory simulations of the expected temporal trends in the photoelectron spectra, eKE(t), and the transformation of the time–energy plot I(eKE, t) in Figure 7(b) into an 'image' of the $A'\ ^2\pi_{1/2}$ IBr^- potential, $E(R)$. Here, we shift focus to the time dependent changes in the PAD and the dual-centre *dynamic* interference description of homonuclear-diatomic dissociation.

6.2. *Dynamic molecular interferometer*

Cohen and Fano commented in 1966 that electrons ionized from homonuclear diatomic molecules, such as N_2 or O_2, should produce 'an interference pattern whose properties depend periodically on the ratio of the internuclear distance to the photoelectron wavelength'.[123] This critical ratio can be varied experimentally in several ways. Cohen and Fano were concerned predominantly with the variations in R/λ_e due to the change in electron wavelength, and the corresponding effects in photoelectron spectroscopic measurements. They concluded that 'this interference may modulate the cross section for photoabsorption by the whole molecule in accordance with (the above) periodicity'.[123]

More recently, Becker and coworkers considered the ionization of diatomic molecules in the context of a molecular 'double-slit' experiment and discussed the oscillations observed in channel-resolved cross-sections attributed to intra-molecular scattering of the emitted electrons.[139–141] In this case once again the variation of R/λ_e tracks the changes in the photoelectron wavelength or momentum, while the internuclear distance parameter, R, remains constant.

The time-resolved photoelectron imaging experiments sampling the photodissociation of homonuclear diatomic anions, such as I_2^-, present a different, *dynamic* perspective of a similar 'double-slit' electron emission process. The fundamental distinction with the

energy (or momentum) domain work by others is that in this case it is the photoelectron wavelength, λ_e, that remains essentially unchanged during the dissociation (at least at relatively long delays), but the internuclear separation R, defining the effective 'arm length' of the interferometer, increases with the experimental delay. Adapting Cohen and Fano's perspective to the present case, the experimental observables are still expected to reflect a periodic dependence on the R/λ_e parameter, but the variation in this ratio is now due primarily to the time-dependent changes in R, not λ_e.

As discussed in Section 6.1, several energy-domain measurements, including the results shown in Figure 7(a), suggested that the dissociation of I_2^- following its 780 nm excitation to the $A'\ ^2\Pi_{g,1/2}$ state occurs on a sub-picosecond time-scale. As an estimate, after 1 ps R reaches ~15 Å; at this distance, all inter-fragment forces are expected to be negligible. It therefore came as a surprise, at first, when the variations in photoelectron anisotropy were found to persist significantly longer, to at least $t = 2.5$ ps (i.e. long after the energy domain dynamics had already ceased).

Shown in Figure 8(a) are the representative 780 nm pump – 390 nm probe photoelectron images of I_2^- obtained at the pump–probe delays indicated.[136] The grey-scale contour plot shown in Figure 8(b) is the time-resolved photoelectron spectrum, $I(\mathrm{eKE},t)$, obtained from the photoelectron images at numerous delays, not just the four shown in Figure 8(a). The plot represents the same dataset as that used in Figure 7(a), but covers a broader delay range. As noted previously, the evolution of the photoelectron spectrum effectively stops after 700–800 fs.[10,135] At longer delays, the peak intensity levels off at $\mathrm{eKE} = 0.12$ eV, which corresponds to the difference between the probe photon energy, 3.18 eV, and the electron affinity of atomic iodine, 3.06 eV. Therefore, the photoelectron band seen at long delays reflects the asymptotic $I(^2P_{3/2}) \leftarrow I^-$ nature of the probe transition. The asymptotic width of the band (full width at half-maximum of 0.05 eV), reflects the probe laser bandwidth convoluted with other broadening factors.

Although it may appear from the energy-domain data that the electronic identity of the I^- fragment in $I_2^- \rightarrow I^- + I(^2P_{3/2})$ photodissociation is established early in the dissociation process, this conclusion is based on the photoelectron spectra only. Time-resolved photoelectron images, such as those in Figure 8(a), contain an additional dimension of information in the angular domain, which was not commented on in the discussion in Section 6.1. The analysis of the images reveals that the evolution of the photoelectron angular distributions continues beyond the initial 700–800 fs timeframe.[136] For example, it can be discerned by careful inspection of Figure 8(a) that the image obtained at a 1650 fs pump–probe delay is more anisotropic than the 550 and 2650 fs images. The persisting changes in the angular distributions suggest that the evolution of the electronic wavefunction continues even after the asymptotic energetic limit of $I_2^- \rightarrow I^- + I(^2P_{3/2})$ photodissociation has been reached, within the experimental resolution. The key to deciphering these dynamics lies, therefore, in the time-resolved photoelectron angular distributions – *not* the energy spectra.

The quantitative analysis of the PADs, described in detail elsewhere,[136] is summarized in Figures 8(b) and (c), which display the delay dependence of the anisotropy parameter $\beta_2(t)$, determined by fitting Equation (2) to the experimental PADs derived from the time-resolved 780 nm pump/390 nm probe photoelectron images. Both Figures 8(b) and (c) display the same $\beta_2(t)$ data, with (c) encompassing a broader delay range. In Figure 8(b), the anisotropy evolution $\beta_2(t)$ is superimposed with the time-resolved photoelectron

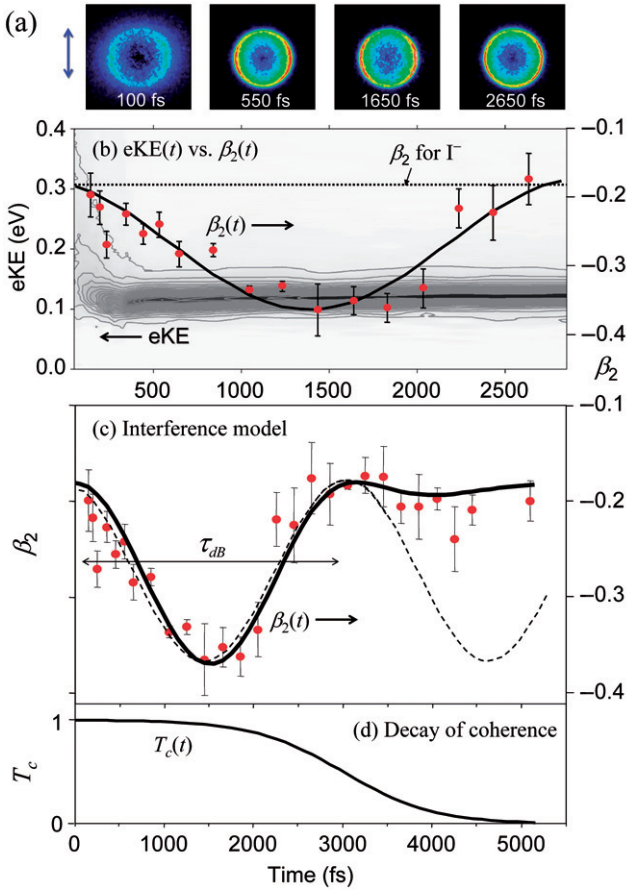

Figure 8. The dynamic molecular interferometer: $I_2^- \rightarrow (I^{-1/2} \cdots I^{-1/2}) \rightarrow I^- + I$, 780 nm pump – 390 nm probe. (a) Representative pump–probe photoelectron images. (b) The time-resolved photoelectron spectrum superimposed with the anisotropy parameter evolution $\beta_2(t)$. Solid curve: interference model. Dotted horizontal line: β_2 for I^- at 390 nm. (c) $\beta_2(t)$ over broader range. Dashed curve: interference model without coherence decay. Solid curve: the Cohen–Fano model. (d) Coherence function with a 3 ps time constant and 0.5 width used for the Cohen–Fano fit.

spectrum in order to emphasize the different time-scales inherent in the angular and energy domains. The error-bars on the plotted β values represent the 95% confidence limits of the experimentally determined mean values. The higher-order moment β_4 in equation (2) is more susceptible to experimental noise, resulting in greater (compared to β_2) errors. Hence, only the β_2 values are plotted in Figure 8. However, the time-scales reflected in the time-dependent angular distributions are adequately represented by $\beta_2(t)$, and therefore reporting only these values is sufficient.

After the completion of the dissociation (at infinitely long delays), the photoelectrons originate from the I^- fragment. Therefore, the alignment with respect to the pump laser polarization is no longer important in the asymptotic data due to the closed-shell, spherically symmetric electronic wavefunction of I^-, resulting in $\beta_4 = 0$. The second

moment, β_2, at long pump–probe delays is expected to converge on that seen in 'static' photodetachment of I^- at the same probe wavelength. The latter is indicated in Figure 8(b) by a dotted horizontal line.[108] The solid curve, drawn through the $\beta_2(t)$ data in Figure 8(b), emphasizes the anisotropy variation on an approximately 2.5 ps time-scale and is intended to guide the eye. The single, most important conclusion from comparison of the $\beta_2(t)$ data in Figure 8(b) to the asymptotic I^- limit is that despite reaching the energetic limit and fairly large fragment separation, the photodetachment in the 1−2 ps delay window does not occur from a final, effectively isolated I^- fragment. In fact, it takes about 2.5 ps for the $\beta_2(t)$ values to return to the value expected from I^-. A separate, relevant piece of the puzzle is found in the observation that the photodetachment anisotropy in the IBr^- case (no equivalent centres) does not exhibit a variation on an extended time-scale under similar experimental conditions, leveling off at the asymptotic I^- level much earlier in the dissociation process.[135,136] Therefore, molecular symmetry resulting in the existence of two fundamentally indistinguishable electron emission centres in the dissociating I_2^- anion is important to understanding the observed anisotropy evolution.

Building on the qualitative picture presented in Section 5.1, the dissociating I_2^- has been described as a *dynamic molecular interferometer* with an effective arm-length R tracking the dissociation progress.[136] The excess electron in $I_2^- \rightarrow I^{-1/2} \cdots I^{-1/2} \rightarrow I^- + I$ dissociation remains *coherently* delocalized between the two I atoms, I_A and I_B. In the present case, the I_2^- $\sigma_u(5p)$ orbital, from which the electron detachment takes place, is described as a linear combination of the $5p$ orbitals of the two dissociating atoms, I_A and I_B: $\sigma_u = c(5p_A + 5p_B)$, where c is a normalization constant. The electronic state symmetry with respect to the operation of inversion is strictly conserved in quantum mechanics and, therefore, the coherently delocalized nature of the excess electron will be preserved, even over large internuclear distances, until an external perturbation scrambles the molecular eigenstates. (In a perfectly isotropic Universe with no external fields, such coherence has no theoretical limit.) As long as coherence is preserved, the electron detachment is subject to interference[123] of two equivalent emission centres:[142]

$$|\psi_f\rangle = c_A|\psi_A\rangle + c_B|\psi_B\rangle, \tag{3}$$

where $|\psi_f\rangle$ is the photodetached electron wavefunction, $|\psi_A\rangle$ and $|\psi_B\rangle$ are waves emitted from I_A and I_B, and the expansion coefficients satisfy the symmetry requirement $|c_A| = |c_B|$. The separation between the two centres is generally described by a nuclear wavepacket. In the semi-classical approximation, it can be set to the value of R obtained from the dissociation trajectory $R(t)$. The experimental observable, $\beta_2(t)$, tracks the variation in the relative phase parameter $R(t)/\lambda_e$, where λ_e is the de Broglie wavelength of the emitted electrons. The ~2.5 ps period seen in Figure 8(b) and (c) then corresponds to $\Delta R \approx \lambda_e$.

Two dynamical time-scales are expected, in general, in a two-centre interference process:[136] the de Broglie time-scale and the excess-electron localization time-scale.

Delocalized-electron dynamics and de Broglie time-scale. Inspection of Figures 8(b) and (c) reveals that the anisotropy parameter completes a full cycle of evolution in about 2.5 ps. A 2.5 ps delay corresponds to an approximately 36 Å separation between the two electron-emission centres, I_A and I_B, which is remarkably similar to the de Broglie wavelength of the asymptotic (eKE = 0.12 eV) photoelectrons, $\lambda_e = 35.4$ Å. Therefore, $\tau_{dB} = 2.5$ ps, referred to as the de Broglie time-scale, couples the dynamics of nuclear

separation and electron emission. Neglecting the initial acceleration and assuming that the fragments separate with a constant relative speed, τ_{dB} is defined as the time, during which the fragments increase their separation by one unit of the effective de Broglie wavelength of the electrons emitted by the subsequent probe pulse. This interval corresponds to the period of interference fringes expected in $\beta_2(t)$.

Since the probe wavelength is orders of magnitude greater than the length scales relevant in the experiment, the photodetachment transition is well described within the electric-dipole approximation. As long as the parent orbital preserves its *ungerade* symmetry, centres I_A and I_B in Equation (3) emit waves with equal amplitudes and the evolution of the PAD reflects the change in the relative phase of $|\psi_A\rangle$ and $|\psi_B\rangle$ observed in the far field. This symmetry-dictated behaviour distinguishes the dissociating I_2^- anion from IBr^-. (In the latter case, the electron localizes on the I^- fragment, as soon as it is dictated by the diabatic excited-state wavefunction. In the absence of the $I^- + Br$ and $I + Br^-$ state degeneracy and quantum symmetry restrictions, the anisotropy variation occurs on the same relatively short time-scale as the energetic or spectral change.)

While in the coherently delocalized electron regime, the phase difference between the equal-amplitude $|\psi_A\rangle$ and $|\psi_B\rangle$ waves is determined, among other factors, by the electron wavelength (λ_e) and $I_A - I_B$ separation (R). From Huygens' point of view, adopted by Cohen and Fano,[123] the anisotropy is expected to display periodicity with respect to R/λ_e. The corresponding delay period should be τ_{dB}. The expected periodicity is illustrated by the dashed line drawn through the $\beta_2(t)$ data in Figure 8(c), which corresponds to the periodic function:

$$\beta_2(t) = a + b\cos\left(\frac{2\pi R(t)}{\lambda_e} + \phi_0\right). \tag{4}$$

This is a first-order, over-simplistic expression, which does not reflect the exact functional form expected for $\beta_2(t)$. Most prominently, it fails to reproduce the decay in $\beta_2(t)$ oscillations at $t > 2.5$ ps. This equation is intended to model only the underlying time-scale and periodicity. It does so by assuming a classical dissociation trajectory $R(t)$, while a and b can be used as adjustable parameters to fit the equation to the experimental data.

The phase factor ϕ_0 in Equation (4) accounts for any phase shift due to the interaction of the emitted electrons with the neutral fragments. If these interactions are neglected by setting $\phi_0 = 0$, the least-squares fit to the data in the $t = 0$ 3 ps range [Figure 8(c)] yields $\lambda_e = 42.7 \pm 1.1$ Å. This value is compared to the 35.4 Å de Broglie wavelength of the 0.12 eV photoelectrons. The observed discrepancy is not trivial and most likely stems from the neglect of the interactions between the photodetached electron and the neutral fragments. Indeed, the expected 35.4 Å wavelength is calculated in the far field, while the relative phase of waves $|\psi_A\rangle$ and $|\psi_B\rangle$ is most susceptible to the electron-neutral interactions in the near field. The effect of these interactions can be accounted for approximately by adopting a non-zero value of ϕ_0 to account to the resulting phase-shift, in which case an adequate fit to the data in the $t = 0$ 3 ps range can be achieved with λ_e at its far-field value, 35.4 Å.[136]

Electron localization and decoherence. The evolution of the anisotropy parameter in the time-revolved imaging measurement of $I_2^- \rightarrow I^{-1/2} \cdots I^{-1/2} \rightarrow I^- + I$ photodissociation also reflects the change in the electronic wavefunction character from that corresponding to the

$A'\ ^2\Pi_{g,1/2}$ molecular state to that with the excess electron localized on one of the final fragments. In the single-electron picture, the wavefunction of the excess electron changes its character from the $\sigma_u(5p)$ molecular orbital (i.e. the doubly occupied HOMO of I_2^- in the $A'\ ^2\Pi_{g,1/2}$ excited state) to a $5p_A$ or $5p_B$ fragment atomic orbital. The importance of this character change in the time-resolved imaging experiments was pointed out by Neumark and coworkers,[10] who proposed that the localization mechanism is likely to involve external-field mixing of the symmetry-adapted molecular eigenstates of gerade and ungerade symmetry, such as $A'\ ^2\Pi_{g,1/2}$ and $X\ ^2\sum_u^+$. The field most likely responsible for the state mixing and eventual electron localization is the DC extraction field within the photoelectron imaging lens.

An estimate of the electron localization time-scale, τ_{loc}, can be obtained as follows.[136] For effective state mixing, the unperturbed $A'\ ^2\Pi_{g,1/2}$ and $X\ ^2\sum_u^+$ potential energy curves must come close enough for the splitting between them to be comparable to the energy difference between the $(I_A + I_B^-)$ and $(I_A^- + I_B)$ localized-electron states in the presence of the external field. While the field-induced perturbation is of the order of $H' = eER$, where E is field intensity, the g–u energy splitting at large internuclear distances should scale as $\Delta E = C/R^4$, corresponding to the charge–induced-dipole interaction between the ionic and neutral fragments. The C coefficient can be estimated from the known 0.8 meV splitting between the $A'\ ^2\Pi_{g,1/2}$ and $X\ ^2\sum_u^+$ states at $R = 13$ Å, as determined by Neumark and coworkers,[10] which yields $C = 23\,\text{eV Å}^4$. Requiring $\Delta E \approx H'$ as a prerequisite for the state mixing, the transition to a localized-electron state is expected in the vicinity of $R \approx (C/eE)^{1/5}$. Under the experimental conditions that apply to Figure 8 (namely, $E = 40$ V/cm), this corresponds to $R \approx 35.6$ Å.[136] By an unintended coincidence, this value is very similar to the de Broglie wavelength of the asymptotic photoelectrons, $\lambda_e = 35.4$ Å. In 780 nm dissociation of I_2, $R = 35.6$ Å is reached at $\tau_{loc} = 2.5$ ps, effectively coinciding with the previously obtained estimate for the de Broglie time-scale, $\tau_{dB} = 2.5$ ps. Although the de Broglie and electron-localization time-scales happen to be similar under the conditions of the I_2^- experiment, they are quite different in their physical nature. While the de Broglie time-scale is defined by the photodissociation and photodetachment energetics, the localization time-scale depends on the external field and molecular potential details.

With the similar values of the de Broglie and localization time-scales, only the first cycle of the interference-induced anisotropy variation is expected (and seen) in Figure 8(c). Due to the low-power scaling of the localization time-scale with the external electric field strength derived above, $\tau_{loc} \propto E^{-1/5}$, the experimental control of this parameter is, unfortunately, not very good: for example, a twofold increase in the imaging field strength (e.g. from 40 to 80 V/cm) shortens the predicted value of τ_{loc} by only 15%. Given the experimental uncertainties, this change is rather small, which may explain why no significant difference was observed between the anisotropy trends in the data obtained with 40 and 80 V/cm imaging fields. However, future experiments with pulsed electron imaging fields are planned to test the field-induced symmetry breaking hypothesis. This approach may provide a way to compare the mixing effects of the external fields of finite (e.g. 40 V/cm) and near-zero strengths.

To summarize, the dissociation process in homonuclear diatomics is not necessarily complete when the peak in the time-resolved photoelectron spectrum reaches the asymptotic eKE value. This common perspective provided by energy domain time-resolved photoelectron spectroscopy does not take into account that for the reaction

to be truly complete, the excess electron must eventually localize on one of the fragments. In the process, it must lose any coherent phase relation with the neutral counterfragment. This transition does not occur on the same time-scale as the energy-domain changes, because it violates molecular symmetry and involves breaking the experimental indistinguishability of the two equivalent fragments, $I_A^{-1/2}$ and $I_B^{-1/2}$. Although the electron has an equal probability of localizing on either of the fragments, the resulting localized wavefunction no longer involves coherence of the two electron-emission centres. In other words, at long delays, the two dissociation limits, $I_A^- + I_B$ and $I_A + I_B^-$, contribute (equally) to the experimental observables without exhibiting quantum interference, because the coherent phase relationship between $|\psi_A\rangle$ and $|\psi_B\rangle$ in Equation (3) at these delays is lost (or, rather, transferred to a greater system including the external fields).[140,142,143]

To avoid possible misconception, we also stress that it is not the act of photodetachment (imaging) measurement that collapses the excess-electron wavefunction ($I_A^{-1/2} + I_B^{-1/2}$) to a localized atomic orbital ($I_A^- + I_B$ or $I_A + I_B^-$). From the quantum-theory point of view, an experiment collapses the wavefunction to an eigenfunction of the operator corresponding to the type of measurement involved. In photoelectron imaging, the measurement is the determination of the position of an electron impact on the detector. The corresponding eigenfunctions are delta-functions of lab-frame coordinates (see Section 2), not the $5p_A$ or $5p_B$ orbitals localized on one of the dissociation fragments. Therefore, the photodetachment probe is not the cause of the excess-electron localization.

The process of electron localization and inter-fragment decoherence can be described by a coherence function $T_c(t)$,[140,141] defined in the spirit of the generalized Cohen–Fano model (developed for the photoionization of symmetric molecules):[123,144,145]

$$T_c(t) = \frac{1}{(1 + \exp -(t - \tau_0)/\Gamma)}. \tag{5}$$

This function is plotted in Figure 8(d), assuming empirically determined values of $\tau_0 = 3$ ps and the width parameter $\Gamma = 0.5$ ps. Note that $\tau_0 = 3$ ps is comparable to $\tau_{loc} = 2.5$ ps estimated above. The plot in Figure 8(d) can be interpreted as the time-dependent degree of either inter-fragment coherence or electron delocalization. The $T_c = 1$ value at short delays corresponds to a delocalized, coherent ($I^{-1/2} \cdots I^{-1/2}$) wavefunction of defined inversion symmetry (*gerade*, for the present case). The asymptotic value of $T_c = 0$, achieved at very long delays, describes the completely separated fragments, $I_A^- + I_B$ or $I_A + I_B^-$, with no coherent phase relationship between them.

Combining the effects of de Broglie periodicity and electron localization/decoherence, the $\beta_2(t)$ variation can be modeled as a periodic wave, whose oscillations are damped in accordance with the assumed coherence function. This approach is similar to that first discussed by Cohen and Fano,[123] even though they considered different experimental observables. Assuming the $T_c(t)$ function plotted in Figure 8(d), the model outcome is shown as a solid curve in Figure 8(c). (In comparing the model prediction to the $\beta_2(t)$ data, the τ_0 and Γ parameters in Equation (5) were adjusted to match the experimental observations.) It is reassuring that the decoherence time $\tau_0 = 3$ ps matches quite closely the 2.5 ps estimate for the electron localization time-scale obtained above by considering the expected *g* and *u* potential scaling and the dipolar interaction with the external field. The overall agreement between the model and the experiment, seen in Figure 8(c),

indicates that the photodetachment of electrons from the dissociating $I_2^- \rightarrow (I^{-1/2} \cdots I^{-1/2})_g \rightarrow I^- + I$ system can indeed be modeled as a dynamic molecular interferometer, while using physically meaningful model parameters.

The de Broglie wavelength effect. In closing, it is instructive to examine the 780 nm pump – 390 nm probe results for I_2^- dissociation[136] in light of the findings by the Neumark group, who used a similar 793 nm excitation wavelength, but probed the dissociation process with the more energetic 265 nm photons.[10] The similarity of the pump wavelengths in the two cases implies similar dissociation dynamics following the excitation to the $A'\,^2\Pi_{g,1/2}$ state of I_2^- see Figure 7(a, left). No other states are expected to be involved and the asymptotic $I^- + I$ fragment separation speeds for the 780 and 793 nm excitations are estimated as 13.3 and 13.0 Å/ps, respectively, indicating only a minor difference between the two experimental regimes. The time-resolved photoelectron energy spectra reported by the two groups[10,131,136] confirm these predictions. Indeed, the most relevant distinction between the 780–390 nm and 793–265 nm time-resolved photoelectron spectra is the difference in photoelectron kinetic energies, attributed to the higher probe photon energy in the latter case. With this caveat, the 390 and 265 nm probes employed in the two experiments sample basically the same dissociation dynamics.

However, a rather different perspective is gained by comparing the 780–390 nm and 793–265 nm time-resolved PADs. Plotted in Figure 9(a) are the evolutions of the anisotropy parameter $\beta_2(t)$ observed in the two regimes. Shown as solid black circles is the 780–390 nm dataset of Mabbs *et al.*,[136] reproduced from Figure 8. Triangles are the 793–265 nm data of Davis *et al.*,[10] with the white and grey symbols representing two independent runs under similar experimental conditions. The figure suggests very different

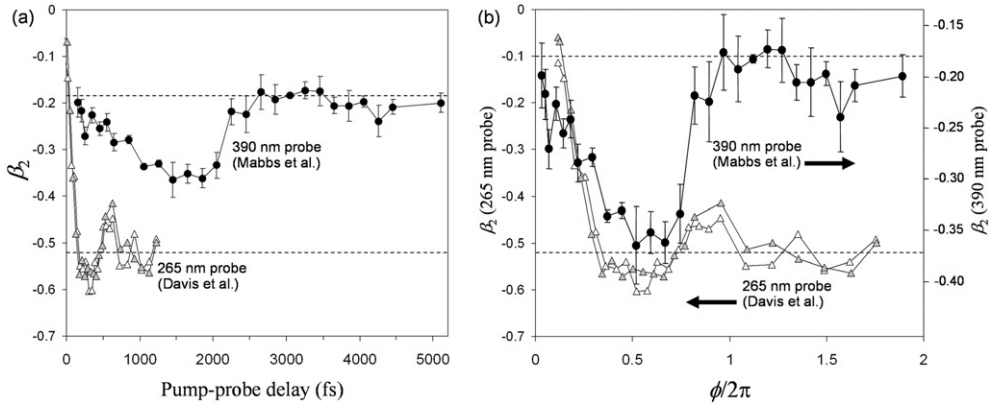

Figure 9. (a) The evolutions of the anisotropy parameter $\beta_2(t)$ observed in two independent time-resolved photoelectron imaging studies of I_2^- photodissociation. Solid black circles: the 780 pump – 390 nm probe data of Mabbs *et al.*,[136] reproduced from Figure 8. Triangles: the 793 pump – 265 nm probe data of Davis *et al.*,[10] with the white and grey symbols representing two independent runs under similar experimental conditions. The dashed horizontal lines indicate the asymptotic β_2 values expected for the final I^- fragments at the respective probe wavelengths. (b) The same β_2 data as in (a), but plotted as functions of the relative phase parameter $\phi = R/\lambda_e + \phi_0$, as defined in the text. Note that different vertical scales are used for the 780 pump – 390 nm probe[136] and 793 pump – 265 nm probe[10] data (the right and left axes, respectively).

behaviours of the photoelectrons detached from essentially the same $I_2^- \rightarrow I^- + I$ system by the 390 and 265 nm probe pulses.

The overall distinction in the β_2 values between the two experiments is expected due to the different eKEs resulting from the 390 and 265 nm probe photons. The dashed horizontal lines in Figure 9(a) indicate the β_2 values for the photodetachment of I^- at the corresponding probe wavelengths. These limits represent the asymptotic anisotropies expected in the photodetachment of the final $I + I^-$ fragments at long pump–probe delays. The most striking and revealing observation in Figure 9(a) is the significant (about a factor of 4) difference in the time-scales of $\beta_2(t)$ variation observed with 390 and 265 nm probe pulses. Naively, this difference might be seen as implying much faster dynamics in the dissociation sampled with the 265 nm probe, compared to 390 nm. This conclusion is in conflict with the common-sense expectation that it is, essentially, the same dissociation process that is being sampled in both the 780–390 nm and 793–265 nm experiments, regardless of the probe wavelength.

The results of the two experiments summarized in Figure 9(a) are easily reconciled using the dual-centre interference picture. As the first hint, the transient maximum at $t = 650$ fs in the Neumark group data corresponds to an internuclear separation of about 11 Å, which compares quite favourably with the 9.7 Å de Broglie wavelength of the 1.6 eV eKE photoelectrons generated by the 265 nm probe. Hence, in this case too, the dissociation and electron emission dynamics appear to be coupled by a common characteristic parameter, the de Broglie wavelength of the photoelectrons. Within the dynamic interferometer description, the two datasets should be compared as functions of the interference parameter R/λ_e, rather than pump–probe delay t. Since the fragment separation speeds are similar in both cases, the slower $\beta_2(t)$ evolution seen in Figure 9(a) for a 390 nm probe, compared to 265 nm, reflects a longer (by a factor of 3.6) de Broglie wavelength of the 390 nm photoelectrons ($\lambda_e = 35.4$ Å vs. 9.7 Å).

In a more quantitative fashion, this point is made in Figure 9(b), where the 265 and 390 nm time-resolved β_2 data are plotted as functions of the relative phase parameter, defined as $\phi = R/\lambda_e + \phi_0$. The additional phase correction, ϕ_0 is added here to the standard interference term R/λ_e to account for any phase shift experienced by the photoelectrons due to their interaction with the neutral fragments. The interaction-induced phase shift is expected to be dependent on de Broglie wavelengths and, therefore, the probe photon energy, necessitating the inclusion of ϕ_0. However, this additional phase results in a shift of the $\beta_2(\phi)$ data along the horizontal axis, while the main conclusion drawn from Figure 9(b) remains unaffected: namely, both the 390 and 265 nm datasets exhibit β_2 variations occurring on similar scales with respect to the relative phase and, therefore, R/λ_e.

For more striking visual comparison, the 265 and 390 nm β_2 values in Figure 9(b) are plotted on separate vertical scales, shown on the left and right vertical axes, respectively. However, we stress again that the absolute values of β_2, on average, reflect mainly the corresponding eKEs. The difference between 265 and 390 nm results in the distinct asymptotic (long delay) values of β_2, as indicated by the dashed horizontal lines in Figure 9(b), similar to Figure 9(a). The dynamic interferometer model does not predict the absolute β_2 values. It does, however, correctly describe the (damped) periodic variations in β_2, which occur with the same *phase* (rather then *time*) period, regardless of the probe wavelength used.

Broader perspective. Thus, when normalized by the de Broglie wavelengths, the evolution of time-resolved photoelectron anisotropy in homonuclear diatomic dissociation reflects the same R/λ_e dependence, regardless of specific experimental conditions. From an even broader perspective, symmetry and symmetry breaking play important roles in quantum dynamics (see Refs.[142,143] for another recent example). The dynamic interference discussed here in the homonuclear diatomic anion context is also a general phenomenon, related by Fourier transform to electron scattering and diffraction in the energy domain.[123,141,146] Conceptually, the described effect is similar to the interference observed in the energy domain in the free-electron waves generated by a pair of identical, delayed femtosecond laser pulses,[147] as well as atom waves generated in the dissociation of neutral diatomics.[148]

The choice of I_2^- for the experiments described in this Section has been dictated by its convenient spectroscopic properties and the large body of previous work on this system, which enabled this work to focus on the physical phenomena, rather than the characterization of the molecular system itself. However, the fundamental property underlying the effect of interference in bond dissociation is rather general – it is symmetry, and not necessarily of the inversion type. The effects described here depend, ultimately, on the existence of two (or, in principle, more) isoenergetic electron emission centres. Therefore, similar issues may arise in a multitude of dimer systems, not necessarily anionic, with neutral $(NO)_2$ being a prominent recent example.[120,149–151]

Looking into the future, we note that dual-centre interference is sensitive not only to the de Broglie wavelength of the photoelectrons and features of the dissociation potential, but also the interactions of the departing electron and the remaining molecular skeleton.[136] Hence, the experiments targeting such interference effects have the potential of delivering details of molecular electronic structures and their transformations in chemical reactions, as well as other types of interactions. This potential is not, by any means, limited to I_2^- used here as a favourite model case.

7. Summary

Photoelectron imaging can be thought of as a quantum photographic technique, focusing on experimental manifestations of quantum mechanics in chemical structures and reaction dynamics and tackling the interplay between electronic and nuclear motions. The images and the interpretative models being developed in the field go beyond current microscopic techniques (such as those in nanotechnology) to provide a conceptual view of bonding structures, which ultimately hold matter together at the most fundamental level. These experiments, therefore, reveal the essence of intra- and inter-molecular interactions and chemical change, relevant to all areas of physical sciences.

The work described here focused on negative ions. In addition to their applied and fundamental importance, anions stand out relative to neutral molecules in that their reactivity is affected much more by interactions with the environment. These interactions are particularly relevant in chemistry, as the diffuse nature of anionic orbitals often renders the excess electron an active player in chemical dynamics and a sensitive probe thereof.

The goals of the photoelectron imaging experiments on negative ions can be summarized as threefold. First, the ‘static’ (one-photon) measurements aim to characterize the anion electronic structure and photodetachment dynamics. Second, the time-resolved

experiments target the electronic transformation effects and excited-state dynamics, observing the bond-breaking in (mostly) unperturbed, isolated molecular anion systems. Third, these structural effects and dynamical processes are examined in microscopic environments, using cluster anions as well-defined study systems.[27,152,153] To this end, the combination of photoelectron imaging with well-established dual time-of-flight photofragment mass-spectrometry[154] is presently emerging as a powerful multi-pronged tool for studying the mechanisms of molecular-level interactions controlling the outcomes of chemical reactions, generally described as solvent-enabled and solvent-controlled chemistry.[117,118]

The future is expected to bring further development of different aspects of the imaging technique and its application to negative ions, including extremely high-resolution imaging,[25] slow photoelectron imaging,[20,155] multiphoton imaging (including its strong-field variant), imaging of pre-aligned molecular anions, many-body coincidence imaging,[69,71,156] to name just a few promising directions. Femtosecond pump–probe photoelectron imaging, particularly its applications to solvated cluster anion systems, is likely to remain at the forefront of the field of time-resolved reaction dynamics.

Acknowledgements

We are indebted to the past and present members of the Sanov group who carried out the original experiments and otherwise contributed to the work cited and described in this paper. They are (in alphabetical order): Ahu Akin, Emily Grumbling, Terefe Habteyes, Kostya Pichugin, Laura Schirra, Eric Surber, Luis Velarde, and Dominique Villela. We are grateful to Dr. Uwe Becker (Fritz-Haber-Institut der Max-Planck-Gesellschaft, Berlin), Dr. Steve Cavanagh and Dr. Steve Gibson (Australian National University) for enlightening discussions and sending us manuscripts prior to their publication. AS acknowledges the generous support in the preparation of this article by the National Science Foundation (grants CHE-0134631 and CHE-0713880) and the David and Lucile Packard Foundation (Fellowship for Science and Engineering). RM gratefully acknowledges the support of the American Chemical Society Petroleum Research Fund (grant 45076-G6).

References

[1]D.W. Chandler and P.L. Houston, J. Chem. Phys. **87**, 1445 (1987).
[2]A.J.R. Heck and D.W. Chandler, Ann. Rev. Phys. Chem. **46**, 335 (1995).
[3]P.L. Houston, Acc. Chem. Res. **28**, 453 (1995).
[4]K.M. Ervin and W.C. Lineberger, in *Advances in Gas Phase Ion Chemistry,* edited by N.G. Adams and L.M. Babcock (JAI Press, Greenwich, 1992), Vol. 1, p. 121.
[5]J.C. Pinaré, B. Baguenard, C. Bordas and M. Broyer, Phys. Rev. Lett. **81**, 2225 (1998).
[6]J.C. Pinaré, B. Baguenard, C. Bordas and M. Broyer, Eur. Phys. J. D **9**, 21 (1999).
[7]B. Baguenard, J.C. Pinaré, C. Bordas and M. Broyer, Phys. Rev. A **63**, 023204 (2001).
[8]E. Surber and A. Sanov, J. Chem. Phys. **116**, 5921 (2002).
[9]E. Surber, R. Mabbs and A. Sanov, J. Phys. Chem. A **107**, 8215 (2003).
[10]A.V. Davis, R. Wester, A.E. Bragg and D.M. Neumark, J. Chem. Phys. **118**, 999 (2003).
[11]H.J. Deyerl, L.S. Alconcel and R.E. Continetti, J. Phys. Chem. A **105**, 552 (2001).
[12]J.R.R. Verlet, A.E. Bragg, A. Kammrath, O. Cheshnovsky and D.M. Neumark, J. Chem. Phys. **121**, 10015 (2004).
[13]D.S. Peterka, A. Lindinger, L. Poisson, M. Ahmed and D.M. Neumark, Phys. Rev. Lett. **91**, 043401 (2003).

[14]A.E. Bragg, J.R.R. Verlet, A. Kammrath, O. Cheshnovsky and D.M. Neumark, J. Chem. Phys. **122**, 054314 (2005).
[15]A.E. Bragg, R. Wester, A.V. Davis, A. Kammrath and D.M. Neumark, Chem. Phys. Lett. **376**, 767 (2003).
[16]A.T.J.B. Eppink and D.H. Parker, Rev. Sci. Instr. **68**, 3477 (1997).
[17]D.H. Parker and A.T.J.B. Eppink, J. Chem. Phys. **107**, 2357 (1997).
[18]M.N. R. Ashfold, N.H. Nahler, A.J. Orr-Ewing, O.P.J. Vieuxmaire, R.L. Toomes, T.N. Kitsopoulos, I.A. Garcia, D.A. Chestakov, S.M. Wu and D.H. Parker, Phys. Chem. Chem. Phys. **8**, 26 (2006).
[19]B.F. Parsons, S.M. Sheehan, K.E. Kautzman, T.A. Yen and D.M. Neumark, J. Chem. Phys. **125**, 244301 (2006).
[20]M.J. Nee, A. Osterwalder, J. Zhou and D.M. Neumark, J. Chem. Phys. **125**, 014306 (2006).
[21]B.F. Parsons, S.M. Sheehan, T.A. Yen, D.M. Neumark, N. Wehre and R. Weinkauf, Phys. Chem. Chem. Phys. **9**, 3291 (2007).
[22]M.S. Bowen and R.E. Continetti, J. Phys. Chem. A **108**, 7827 (2004).
[23]G.J. Rathbone, T. Sanford, D. Andrews and W.C. Lineberger, Chem. Phys. Lett. **401**, 570 (2005).
[24]M.A. Sobhy and A.W. Castleman, J. Chem. Phys. **126**, 154314 (2007).
[25]S.J. Cavanagh, S.T. Gibson, M.N. Gale, C.J. Dedman, E.H. Roberts and B.R. Lewis, Phys. Rev. A **76**, 052708 (2007).
[26]G.R. Fleming and P.G. Wolynes, Phys. Today **43**, 36 (1990).
[27]A.W. Castleman and K.H. Bowen, J. Phys. Chem. **100**, 12911 (1996).
[28]D.M. Neumark, Ann. Rev. Phys. Chem. **52**, 255 (2001).
[29]A. Stolow, A.E. Bragg and D.M. Neumark, Chem. Rev. **104**, 1719 (2004).
[30]T. Suzuki, Ann. Rev. Phys. Chem. **57**, 555 (2006).
[31]L. Wang, H. Kohguchi and T. Suzuki, Faraday Disc. **113**, 37 (1999).
[32]S. Lochbrunner, J.J. Larsen, J.P. Shaffer, M. Schmitt, T. Schultz, J.G. Underwood and A. Stolow, J. Electron Spectrosc. Relat. Phenom. **112**, 183 (2000).
[33]T. Seideman, J. Chem. Phys. **113**, 1677 (2000).
[34]V. Blanchet, S. Lochbrunner, M. Schmitt, J.P. Shaffer, J.J. Larsen, M.Z. Zgierski, T. Seideman and A. Stolow, Faraday Disc. **115**, 33 (2000).
[35]T. Seideman, J. Chem. Phys. **107**, 7859 (1997).
[36]M. Tsubouchi, B.J. Whitaker, L. Wang, H. Kohguchi and T. Suzuki, Phys. Rev. Lett. **86**, 4500 (2001).
[37]Y. Arasaki, K. Takatsuka, K.H. Wang and V. McKoy, J. Electron Spectrosc. Relat. Phenom. **108**, 89 (2000).
[38]K. Takatsuka, Y. Arasaki, K. Wang and V. McKoy, Faraday Disc. **115**, 1 (2000).
[39]R.L. Dubs and V. McKoy, J. Chem. Phys. **91**, 5208 (1989).
[40]H. Rudolph and V. McKoy, J. Chem. Phys. **91**, 2235 (1989).
[41]S.N. Dixit, D.L. Lynch, V. McKoy and W.M. Huo, Phys. Rev. A **32**, 1267 (1985).
[42]P. Cong, A. Mokhtari and A.H. Zewail, Chem. Phys. Lett. **172**, 109 (1990).
[43]M. Gruebele and A.H. Zewail, J. Chem. Phys. **98**, 883 (1993).
[44]T.S. Rose, M.J. Rosker and A.H. Zewail, J. Chem. Phys. **88**, 6672 (1988).
[45]N.F. Scherer, R.J. Carlson, A. Matro, M. Du, A.J. Ruggiero, V. Romero-Rochin, J.A. Cina, G.R. Fleming and S.A. Rice, J. Chem. Phys. **95**, 1487 (1991).
[46]N.F. Scherer, D.M. Jonas and G.R. Fleming, J. Chem. Phys. **99**, 153 (1993).
[47]J.M. Papanikolas, R.M. Williams and S.R. Leone, J. Chem. Phys. **107**, 4172 (1997).
[48]I.S. Averbukh, M.J. J. Vrakking, D.M. Villeneuve and A. Stolow, Phys. Rev. Lett. **77**, 3518 (1996).
[49]N. Pugliano, D.K. Palit, A.Z. Szarka and R.M. Hochstrasser, J. Chem. Phys. **99**, 7273 (1993).
[50]U. Banin, R. Kosloff and S. Ruhman, Isr. J. Chem. **33**, 141 (1993).
[51]U. Banin, R. Kosloff and S. Ruhman, Isr. J. Chem. **33**, 141 (1993).

[52]A. Sanov, T. Sanford, L.J. Butler, J. Vala, R. Kosloff and W.C. Lineberger, J. Phys. Chem. A **103**, 10244 (1999).
[53]T. Seideman, Phys. Rev. Lett. **83**, 4971 (1999).
[54]Y. Arasaki, K. Takatsuka, K. Wang and V. McKoy, J. Chem. Phys. **112**, 8871 (2000).
[55]A.M. Rijs, E.H. G. Backus, C.A. de Lange, M.H. M. Janssen, K. Wang and V. McKoy, J. Chem. Phys. **114**, 9413 (2001).
[56]Y. Arasaki, K. Takatsuka, K. Wang and V. McKoy, J. Chem. Phys. **114**, 7941 (2001).
[57]J.A. Davies, R.E. Continetti, D.W. Chandler and C.C. Hayden, Phys. Rev. Lett. **84**, 5983 (2000).
[58]T. Droz-Georget, M. Zyrianov, H. Reisler and D.W. Chandler, Chem. Phys. Lett. **276**, 5 (1997).
[59]X.H. Liu, R.L. Gross and A.G. Suits, Science **294**, 2527 (2001).
[60]D. Townsend, W. Li, S.K. Lee, R.L. Gross and A.G. Suits, J. Phys. Chem. A **109**, 8661 (2005).
[61]M.J. Bass, M. Brouard, A.P. Clark and C. Vallance, J. Chem. Phys. **117**, 8723 (2002).
[62]C. Vallance, M. Brouard, M.J. Bass, A.P. Clark and B.M. Haya, Abstr. Pap. Am. Chem. Soc. **227**, U247 (2004).
[63]P.L. Houston, J. Phys. Chem. **100**, 12757 (1996).
[64]W. Li, C.S. Huang, M. Patel, D. Wilson and A. Suits, J. Chem. Phys. **124**, 011102 (2006).
[65]J.J. Lin, J.G. Zhou, W.C. Shiu and K.P. Liu, Science **300**, 966 (2003).
[66]T.G. Clements, A.K. Luong, H.J. Deyerl and R.E. Continetti, J. Chem. Phys. **114**, 8436 (2001).
[67]C.R. Sherwood, K.A. Hanold, M.C. Garner, K.M. Strong and R.E. Continetti, J. Chem. Phys. **105**, 10803 (1996).
[68]C.R. Sherwood and R.E. Continetti, Chem. Phys. Lett. **0258**, 171 (1996).
[69]R.E. Continetti, Ann. Rev. Phys. Chem. **52**, 165 (2001).
[70]T.G. Clements and R.E. Continetti, Phys. Rev. Lett. **89**, 033005 (2002).
[71]J.A. Davies, J.E. LeClaire, R.E. Continetti and C.C. Hayden, J. Chem. Phys. **111**, 1 (1999).
[72]T.N. Kitsopoulos, C.R. Gebhardt and T.P. Rakitzis, J. Chem. Phys. **115**, 9727 (2001).
[73]C.R. Gebhardt, T.P. Rakitzis, P.C. Samartzis, V. Ladopoulos and T.N. Kitsopoulos, Rev. Sci. Instr. **72**, 3848 (2001).
[74]D. Townsend, M.P. Minitti and A.G. Suits, Rev. Sci. Instr. **74**, 2530 (2003).
[75]D. Townsend, S.K. Lee and A.G. Suits, J. Phys. Chem. A **108**, 8106 (2004).
[76]D.A. Chestakov, S.M. Wu, G.R. Wu, D.H. Parker, A.T. J. B. Eppink and T.N. Kitsopoulos, J. Phys. Chem. A **108**, 8100 (2004).
[77]W. Li, S.D. Chambreau, S.A. Lahankar and A.G. Suits, Rev. Sci. Instr. **76**, 063106 (2005).
[78]V. Dribinski, A. Ossadtchi, V.A. Mandelshtam and H. Reisler, Rev. Sci. Instr. **73**, 2634 (2002).
[79]S. Manzhos and H.P. Loock, Rev. Sci. Instr. **75**, 2435 (2004).
[80]S. Manzhos and H.P. Loock, Comput Phys Commun **154**, 76 (2003).
[81]G.A. Garcia, L. Nahon and I. Powis, Rev. Sci. Instr. **75**, 4989 (2004).
[82]J. Cooper and R.N. Zare, in *Atomic Collision Processes,* edited by S. Geltman, K.T. Mahanthappa, and W.E. Brittin (Gordon and Breach, Science Publishers, New York, London, Paris, 1968), Vol. XI-C, p. 317.
[83]T. Tsukuda, T. Hirose and T. Nagata, Chem. Phys. Lett. **279**, 179 (1997).
[84]D. Dill and J.L. Dehmer, J. Chem. Phys. **61**, 692 (1974).
[85]D. Dill, J. Chem. Phys. **65**, 1130 (1976).
[86]S.N. Dixit and V. Mckoy, J. Chem. Phys. **82**, 3546 (1985).
[87]J.L. Dehmer and D. Dill, Phys. Rev. A **18**, 164 (1978).
[88]J. Cooper and R.N. Zare, J. Chem. Phys. **49**, 4252 (1968).
[89]T. Seideman, Ann. Rev. Phys. Chem. **53**, 41 (2002).
[90]H. Park and R.N. Zare, J. Chem. Phys. **104**, 4554 (1996).
[91]C.M. Oana and A.I. Krylov, J. Chem. Phys. (in press).
[92]K.J. Reed, A.H. Zimmerman, H.C. Andersen and J.I. Brauman, J. Chem. Phys. **64**, 1368 (1976).
[93]E.P. Wigner, Phys. Rev. **73**, 1002 (1948).

[94]R.D. Mead, K.R. Lykke and W.C. Lineberger, in *Electronic and Atomic Collisions,* edited by J. Eichler, I.V. Hertel, and N. Stolterfoht (Elsevier, Amsterdam, 1984), p. 721.
[95]F.A. Akin, L.K. Schirra and A. Sanov, J. Phys. Chem. A **110**, 8031 (2006).
[96]L. Velarde, T. Habteyes, E. Grumbling, K. Pichugin and A. Sanov, J. Chem. Phys. **127**, 084302 (2007).
[97]J. Cooper and R.N. Zare, J. Chem. Phys. **48**, 942 (1968).
[98]C. Bordas, J.C. Pinaré, B. Baguenard and M. Broyer, J. Phys. IV **10**, 55 (2000).
[99]A.E. Bragg, J.R. R. Verlet, A. Kammrath, O. Cheshnovsky and D.M. Neumark, Science **306**, 669 (2004).
[100]A.E. Bragg, J.R. R. Verlet, A. Kammrath, O. Cheshnovsky and D.M. Neumark, J. Am. Chem. Soc. **127**, 15283 (2005).
[101]J.R. R. Verlet, A.E. Bragg, A. Kammrath, O. Cheshnovsky and D.M. Neumark, Science **307**, 93 (2005).
[102]A.A. Hoops, J.R. Gascooke, A.E. Faulhaber, K.E. Kautzman and D.M. Neumark, Chem. Phys. Lett. **374**, 235 (2003).
[103]E. Surber and A. Sanov, J. Chem. Phys. **118**, 9192 (2003).
[104]R. Mabbs, E. Surber and A. Sanov, Analyst **128**, 765 (2003).
[105]E. Surber and A. Sanov, Phys. Rev. Lett. **90**, 093001 (2003).
[106]R. Mabbs, E. Surber and A. Sanov, Chem. Phys. Lett. **381**, 479 (2003).
[107]R. Mabbs, E. Surber, L. Velarde and A. Sanov, J. Chem. Phys. **120**, 5148 (2004).
[108]R. Mabbs, E. Surber and A. Sanov, J. Chem. Phys. **122**, 054308 (2005).
[109]E. Surber, R. Mabbs, T. Habteyes and A. Sanov, J. Phys. Chem. A **109**, 4452 (2005).
[110]J.W. Farley, Phys. Rev. A **40**, 6286 (1989).
[111]D. Serxner, C.E. H. Dessent and M.A. Johnson, J. Chem. Phys. **105**, 7231 (1996).
[112]B. Baguenard, J.C. Pinaré, F. Lépine, C. Bordas and M. Broyer, Chem. Phys. Lett. **352**, 147 (2002).
[113]A.E. Bragg, J.R. R. Verlet, A. Kammrath and D.M. Neumark, J. Chem. Phys. **121**, 3515 (2004).
[114]S.H. Fleischman and K.D. Jordan, J. Phys. Chem. **91**, 1300 (1987).
[115]A. Sanov, W.C. Lineberger and K.D. Jordan, J. Phys. Chem. A **102**, 2509 (1998).
[116]A. Sanov, S. Nandi, K.D. Jordan and W.C. Lineberger, J. Chem. Phys. **109**, 1264 (1998).
[117]L. Velarde, T. Habteyes and A. Sanov, J. Chem. Phys. **125**, 114303 (2006).
[118]T. Habteyes, L. Velarde and A. Sanov, Chem. Phys. Lett. **424**, 268 (2006).
[119]T. Suzuki, L. Wang and H. Kohguchi, J. Chem. Phys. **111**, 4859 (1999).
[120]O. Gessner, A.M. D. Lee, J.P. Shaffer, H. Reisler, S.V. Levchenko, A.I. Krylov, J.G. Underwood, H. Shi, A.L. L. East, D.M. Wardlaw, E.T. Chrysostom, C.C. Hayden and A. Stolow, Science **311**, 219 (2006).
[121]C. Joensson, Z. Phys. **161**, 454 (1961).
[122]U. Fano, Phys. Rev. **1**, 1866 (1961).
[123]H.D. Cohen and U. Fano, Phys. Rev. **150**, 30 (1966).
[124]G. Bilalbegovic, Chem. Phys. Lett. **441**, 309 (2007).
[125]M.J. DeLuca, B. Niu and M.A. Johnson, J. Chem. Phys. **88**, 5857 (1988).
[126]T. Tsukuda, M.A. Johnson and T. Nagata, Chem. Phys. Lett. **268**, 429 (1997).
[127]J.W. Shin, N.I. Hammer, M.A. Johnson, H. Schneider, A. Gloss and J.M. Weber, J. Phys. Chem. A **109**, 3146 (2005).
[128]M.J. S. Dewar, Proc. Cambridge Phil. Soc. **45**, 638 (1949).
[129]T. Habteyes, L. Velarde, and A. Sanov (in preparation).
[130]L.A. Yu, A.H. Zeng, Q.A. Xu and M.F. Zhou, J. Phys. Chem. A **108**, 8264 (2004).
[131]B.J. Greenblatt, M.T. Zanni and D.M. Neumark, Chem. Phys. Lett. **258**, 523 (1996).
[132]B.J. Greenblatt, M.T. Zanni and D.M. Neumark, Science **276**, 1675 (1997).
[133]J.S. Baskin and A.H. Zewail, J. Chem. Educ. **78**, 737 (2001).
[134]R. Mabbs, K. Pichugin, E. Surber and A. Sanov, J. Chem. Phys. **121**, 265 (2004).

[135]R. Mabbs, K. Pichugin and A. Sanov, J. Chem. Phys. **122**, 174305 (2005).
[136]R. Mabbs, K. Pichugin and A. Sanov, J. Chem. Phys. **123**, 054329 (2005).
[137]M.T. Zanni, V.S. Batista, B.J. Greenblatt, W.H. Miller and D.M. Neumark, J. Chem. Phys. **110**, 3748 (1999).
[138]T. Sanford, S.-Y. Han, M.A. Thompson, R. Parson and W.C. Lineberger, J. Chem. Phys. **122**, 054307 (2005).
[139]D. Rolles, M. Braune, S. Cvejanovic, O. Gessner, R. Hentges, S. Korica, B. Langer, T. Lischke, G. Prumper, A. Reinkoster, J. Viefhaus, B.R. Zimmermann, V. McKoy and U. Becker, Nature **437**, 711 (2005).
[140]U. Becker, J. Electron Spectrosc. Relat. Phenom. **156**, Xxiii (2007).
[141]B. Zimmermann, D. Rolles, B. Langer, R. Hentges, M. Braune, S. Cvejanovic, O. Geßner, F. Heiser, S. Korica, T. Lischke, G. Prümper, A. Reinköster, J. Viefhaus, R. Dörner, V. McKoy, and U. Becker, manuscript in preparation.
[142]A. Sanov, Science **315**, 610 (2007).
[143]F. Martin, J. Fernandez, T. Havermeier, L. Foucar, T. Weber, K. Kreidi, M. Schoffler, L. Schmidt, T. Jahnke, O. Jagutzki, A. Czasch, E.P. Benis, T. Osipov, A.L. Landers, A. Belkacem, M.H. Prior, H. Schmidt-Bocking, C.L. Cocke and R. Dorner, Science **315**, 629 (2007).
[144]O.A. Fojon, J. Fernandez, A. Palacios, R.D. Rivarola and F. Martin, J. Phys. B **37**, 3035 (2004).
[145]J. Fernandez, O. Fojon, A. Palacios and F. Martin, Phys. Rev. Lett. **98**, 043005 (2007).
[146]U. Becker, O. Gessner and A. Rudel, J. Electron Spectrosc. Relat. Phenom. **108**, 189 (2000).
[147]M. Wollenhaupt, A. Assion, D. Liese, C. Sarpe-Tudoran, T. Baumert, S. Zamith, M.A. Bouchene, B. Girard, A. Flettner, U. Weichmann and G. Gerber, Phys. Rev. Lett. **89**, 173001 (2002).
[148]C. Petersen, E. Peronne, J. Thogersen, H. Stapelfeldt and M. Machholm, Phys. Rev. A **70**, 033404 (2004).
[149]S.V. Levchenko, H. Reisler, A.I. Krylov, O. Gessner, A. Stolow, H.C. Shi and A.L. L. East, J. Chem. Phys. **125**, 084301 (2006).
[150]V. Dribinski, A.B. Potter, I. Fedorov and H. Reisler, J. Chem. Phys. **121**, 12353 (2004).
[151]V. Dribinski, A.B. Potter, I. Fedorov and H. Reisler, Chem. Phys. Lett. **385**, 233 (2004).
[152]A. Sanov and W.C. Lineberger, Phys. Chem. Comm. **5**, 165 (2002).
[153]A. Sanov and W.C. Lineberger, Phys. Chem. Chem. Phys. **6**, 2018 (2004).
[154]M.A. Johnson and W.C. Lineberger, in *Techniques for the Study of Ion Molecule Reactions*. edited by J.M. Farrar and W.H. Saunders (Wiley, New York, 1988), p. 591.
[155]A. Osterwalder, M.J. Nee, J. Zhou and D.M. Neumark, J. Chem. Phys. **121**, 6317 (2004).
[156]M.S. Bowen, M. Becucci and R.E. Continetti, J. Phys. Chem. A **109**, 11781 (2005).